

# Investigations on Hydrocarbon Compounds in a Pulsed Discharge Nozzle using REMPI

---

Master's Thesis for the Degree of Master of Science

by

Sebastian Schwetje

**Supervisors:**

Prof. Dr. Thomas Giesen

Prof. Dr. Jochen Mikosch

Study Program: Nanoscience

University of Kassel

FB 10 - Mathematik und Naturwissenschaften

Experimentalphysik V - Laborastrophysik

Submission Date: 03.03.2025

# Contents

<b>1</b>	<b>Abstract</b>	<b>1</b>
<b>2</b>	<b>Introduction</b>	<b>2</b>
<b>3</b>	<b>Fundamentals</b>	<b>4</b>
3.1	Diffuse Interstellar bands . . . . .	4
3.2	The molecular beam source . . . . .	4
3.2.1	Supersonic expansion . . . . .	5
3.2.2	Electrical discharges . . . . .	8
3.3	Molecular spectroscopy . . . . .	11
3.3.1	Rotational spectroscopy . . . . .	11
3.3.2	Vibrational spectroscopy . . . . .	13
3.3.3	Electronic spectroscopy . . . . .	15
3.4	Resonance-enhanced multi-photon ionization . . . . .	17
3.5	Mass spectrometry . . . . .	18
3.6	Mass calibration . . . . .	21
<b>4</b>	<b>Experimental</b>	<b>22</b>
4.1	Experimental setup . . . . .	22
4.1.1	Expansion . . . . .	22
4.1.2	Interaction chamber . . . . .	22
4.1.3	The Even-Lavie valve . . . . .	24
4.2	Radiation source . . . . .	26
4.3	Data acquisition . . . . .	27
<b>5</b>	<b>Results and evaluation</b>	<b>28</b>
5.1	Acetylene . . . . .	29
5.2	Diacetylene . . . . .	36
5.3	Density variations . . . . .	38
5.4	Voltage variations . . . . .	44
<b>6</b>	<b>Discussion</b>	<b>46</b>
<b>7</b>	<b>Conclusion and Outlook</b>	<b>51</b>

## List of Figures

1	Scheme of a supersonic expansion through a small nozzle . . . . .	7
2	Exploded view of the mountable discharge nozzle . . . . .	9
3	Formation of different regions during a discharge in a gas-filled discharge tube . . . . .	10
4	Electron avalanche during an electrical discharge . . . . .	10
5	Multi-photon ionization (MPI) and resonance-enhanced multi-photon ionization (REMPI) schemes . . . . .	18
6	Schematic representation of a Wiley-McLaren time-of-flight mass spectrometer . . . . .	20
7	Experimental setup . . . . .	23
8	Cross section of the Even-Lavie valve . . . . .	25
9	Mass spectrum of 2 % acetylene in helium in a discharge with an opening time of $40\mu\text{s}$ , 5 bars of backing pressure and a voltage of 900 V with background subtraction . . . . .	30
10	Mass spectrum of 0.5 % acetylene in helium in a discharge with an opening time of $28\mu\text{s}$ , 10 bars of backing pressure and a discharge voltage of 1100 V with background subtraction . . . . .	31
11	2+1-REMPI spectrum of acetylene from $71700$ to $84200\text{ cm}^{-1}$ . . . . .	34
12	1+1-REMPI spectrum of diacetylene from $40500$ to $46500\text{ cm}^{-1}$ . . . . .	37
13	Amounts of acetylene, diacetylene and helium within the gas pulse for varying nozzle opening times and backing pressures . . . . .	42
14	Total diacetylene yields with different nozzle opening times at varying backing pressures . . . . .	43
15	Helium und diacetylene yields in dependence of applied voltage . . . . .	44

---

## List of Tables

1	Vibrational modes for acetylene in its electronic ground state . . . . .	14
2	Intensities for visible peaks in the mass spectrum shown in Figure 9 . . .	31
3	Intensities for visible peaks in the mass spectrum shown in Figure 10 . . .	32
4	List of acetylene peaks with assignments . . . . .	35
5	List of diacetylene peaks with assignments . . . . .	36

## Abbreviations

2PI - two-photon ionization

DC - direct current DIB - diffuse interstellar band

IE - ionization energy

MPI - multi-photon ionization

PAH - polycyclic aromatic hydrocarbon

REMPI - resonance-enhanced multi-photon ionization

SHV - safe high voltage

ToF - time of flight

UHV - Ultra high vacuum

VUV - vacuum ultraviolet

## 1 Abstract

In this work, the Even-Lavie valve mounted with a DC discharge nozzle is utilized to generate a molecular beam within a vacuum chamber setup. A Wiley-McLaren type mass spectrometer, which is coupled with a tunable wavelength picosecond laser allows the detection of molecules within the beam by employing resonance-enhanced multi-photon ionization (REMPI). The precursor molecule in this work is acetylene, which is discharged during a supersonic expansion to form transient hydrocarbon species. Subsequent to a spectroscopic identification of acetylene and diacetylene, the discharge parameters like pressure, nozzle opening time and voltage are varied and the results are presented.

## 2 Introduction

Hydrocarbon compounds play an important role across a variety of scientific fields, including astrochemistry, combustion studies, and plasma physics. These molecules are crucial for understanding fundamental processes as they undergo complex chemical reactions in diverse environments, such as interstellar space or combustion engines. Indeed, many molecules in the interstellar medium have been identified as hydrocarbon species, making the study of transient hydrocarbons essential for understanding the complex reactions in space. Furthermore, the study of transient hydrocarbons contributes to the understanding of diffuse interstellar bands (DIBs), whose origins remain a widely unsolved mystery for over 100 years [1].

One of the key techniques used to investigate these species is resonance-enhanced multiphoton ionization (REMPI), in conjunction with a time-of-flight mass spectrometer. This method provides a highly selective and sensitive approach for ionizing and detecting molecules. A pulsed discharge nozzle enables the production of these transient species within controlled laboratory conditions. Nevertheless, due to the complexity of discharge processes the generation and characterization of these short-lived molecules remain challenging.

A variety of precursor molecules have been utilized in discharge experiments with different analysis techniques. The discharge products of benzene alone, or in combination with molecular oxygen or nitrogen have been characterized using microwave spectroscopy in a cavity [2]. The study of McCarthy et al. was able to identify over 152 distinct species including masses that exceed those of the precursor molecule benzene, providing valuable insights into the rich carbon chemistry happening during the discharge process. Other works employed a pulsed F<sub>2</sub>-excimer laser to ionize intermediate species from acetylene plasma created by a general valve in combination with a DC discharge [3]. Their results showed that discharging acetylene predominantly leads to the formation of hydrocarbon species with an even amount of carbon atoms with diacetylene being the most abundant. The C<sub>2</sub>H radical was hypothesized to be the driving force behind the carbon chain polymerization mechanism, which has been studied extensively by Laufer et al. [4], even though C<sub>2</sub>H could not be observed directly due to its high reactivity.

This thesis is focused on the investigation of hydrocarbon species formed in a pulsed discharge nozzle using REMPI. As precursor molecule, acetylene diluted in helium is used while important parameters like nozzle opening time, backing pressure and voltage are varied systematically. An electronic spectrum generated from a broadband scan pro-

---

vides an overview of electronic transitions, which in turn can be used to identify specific molecules and to optimize the production conditions. First a theoretical background about supersonic expansions, molecular beams, mass and molecular spectroscopy, and REMPI is given. In Chapter 4 the setup of the pulsed discharge nozzle together with the vacuum chamber and data acquisition are described. This is followed by the presentation and evaluation of the experimental data. The findings are then interpreted and discussed in Chapter 6. Upon these findings, discharge experiments with more complex precursor molecules such as benzene can be conducted in the future, contributing to the identification of DIBs and to provide a more comprehensive understanding of the rich carbon chemistry occurring in space.

## 3 Fundamentals

### 3.1 Diffuse Interstellar bands

Diffuse interstellar bands (DIBs) are absorption features of currently unknown origin observed primarily in the visible and near-infrared spectrum of interstellar objects or galaxies. These features are speculated to arise from molecules in the interstellar medium which absorb light from a given stellar object and therefore appear as absorption lines in the spectra of numerous stellar objects in both our galaxy and other galaxies [1]. Since their discovery by Mary Lea Heger in 1922, who initially identified unexplained absorption features in her observations of some stellar spectra, the number of DIBs has continuously increased to exceed 550 features, as documented in the Apache Point Observatory Catalog of Optical Diffuse Interstellar Bands [5]. Except for a recent breakthrough on DIB carrier molecules where  $C_{60}^+$  has been identified as a viable carrier of several near-infrared DIBs, marking a major breakthrough on this topic, no other molecules have been identified to date [6]. Large organic molecules, such as polycyclic aromatic hydrocarbons (PAHs), fullerenes like  $C_{60}^+$ , and prebiotic or other carbon-based molecules, have been proposed as promising candidates to carry DIBs. Of these, especially PAHs have gotten particular attention, due to their high abundance in space and their stability against photo- and thermodissociation. This renders them strong contenders in the quest for DIBs [7]. DIBs vary in strength depending on density and composition of interstellar clouds, providing valuable insight into the chemistry of the interstellar medium. They have been observed not only in the Milky Way but also in other galaxies, suggesting the processes responsible for DIBs are present throughout the universe. The combination of high-resolution spectroscopy and the utilization of space telescopes, such as the Hubble Space Telescope for ultraviolet, visible and near-infrared wavelengths, or the James Webb Space Telescope (JWST) for orange to mid-infrared wavelengths, fundamental questions concerning the origins of life or the development of the universe can be investigated further. However, despite a century of research in that domain, the majority of the DIB carriers still remain elusive.

### 3.2 The molecular beam source

Molecular beams are defined as directed beams of neutral or ionized molecules at sufficiently low pressures that molecular collisions become negligible. A notable historic experiment that employed a molecular beam was the Stern-Gerlach experiment [8]. In

this experiment, a beam of silver atoms from a heated steel crucible was directed through an orifice, passed an inhomogeneous magnetic field and was targeted onto a glass plate. The formation of two separate silver spots on the plate depending on their magnetic moment ultimately led to the discovery of the spatial quantization of angular momentum. Nowadays, molecular beams have found technical application in molecular beam epitaxy (MBE), utilized in the fabrication of thin films, fabrication of quantum wells, wires or dots. They also find scientific application in scattering experiments as well as single- and crossed-beam methods [9].

As previously stated, the pressure within the chamber must be sufficiently low to minimize collisions between molecules in the beam. This is typically achieved by pumping the chamber with vacuum pumps, often in unison with cold traps, down to pressures of  $10^{-5}$  mbar and below. Since the 1970s, the molecular beam technique has been further developed towards the supersonic beam technique, which enables the use of higher source pressures and thus higher molecule densities [10]. A gas expanding into a lower pressure regime can be approximated as an isenthalpic expansion. Ideally, no heat is exchanged with the surroundings. The work done in the gas expansion is drawn from the internal energy of the gas, which in turn results in a drop in temperature. Molecular rotation can be cooled more efficiently through collisions compared to molecular vibration, meaning the supersonic expansion can produce highly cooled molecules, which are beneficial for applications such as molecular spectroscopy. Seeding the molecules with either a lighter or heavier carrier gas can further influence beam properties like terminal beam velocity or beam temperature. A more thorough explanation about the mechanism of a supersonic expansion will be given in Chapter 3.2.1.

### 3.2.1 Supersonic expansion

The Even-Lavie nozzle, equipped with a mountable discharge nozzle is able to create a supersonic expansion, that efficiently cools molecular species down to several K. This temperature comes close to the temperature of the interstellar medium, molecular clouds in particular. As the objective of this work is to create transient species in a discharge, not only the temperature is important, but also the amount of interaction between molecules. A supersonic expansion as shown in Figure 1 occurs when a gas flows from a high-pressure region to a low-pressure region, where the speed of sound is lower [11], therefore achieving high Mach numbers. Here, the nozzle acts as an orifice which separates

the high-pressure region from the low-pressure region. During this work, the nozzle was operated at 1-10 bar backing pressure and expanded into a low-pressure region in the  $10^{-7}$  to low  $10^{-5}$  mbar regime. When entering the low-pressure region, the gas expands in a continuum regime while rapidly decreasing in density. This region is also called 'zone of action' [11][12]. After passing a 'quitting surface' a transition to free-molecular flow occurs, entering the 'zone of silence'. Within the zone of silence, the expansion remains undisturbed reaching Mach numbers much greater than 1 and not allowing any inter-molecular interaction. Zone of action and zone of silence together form the Mach cone, whose borders are referred to as Mach disc. Beyond the Mach disc, the Mach number drops below one again, which is visible as barrel shock and marks the border where the expansion is no longer undisturbed. A skimmer is inserted right into the zone of silence further perturbing the expansion but allowing to extract a portion of the expanding gas which has already cooled down and does not interact with itself anymore. The extracted portion is now narrowed down and has low density, but also a mostly uniform velocity distribution eliminating most of a potential Doppler broadening. The collision frequency of molecules in a molecular beam has been described more thoroughly by Lubman et al. in 1982 [13].

One model to describe a supersonic expansion is the isentropic expansion model. It can be derived from the equation for a reversible (no entropy change,  $\Delta S = 0$ ), adiabatic (no heat exchange,  $\Delta Q = 0$ ) process [14], where  $p$  denotes the gas pressure,  $V$  denotes the volume of the gas, and  $\gamma$  denotes the heat capacity ratio of the gas

$$pV^\gamma = \text{const.} \quad (1)$$

Using the ideal gas equation and solving it for the volume  $V$  gives

$$V = \frac{nRT}{p} \quad (2)$$

with  $n$  as the molar number,  $R$  as the molar gas constant and  $T$  as the temperature. Substituting this into Equation 1 gives

$$p \frac{(nRT)^\gamma}{p^\gamma} = \text{const.}, \quad (3)$$

where  $n$  and  $R$  are constants further reducing the equation to

$$p^{1-\gamma} T^\gamma = \text{const.} \quad (4)$$

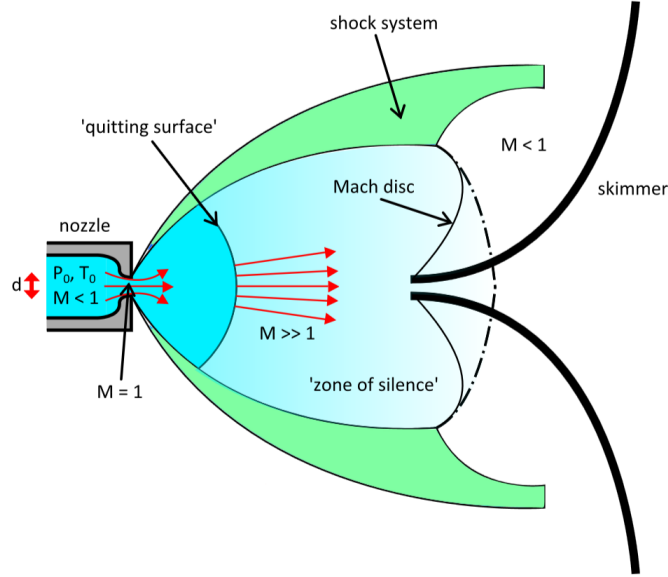


Figure 1: Scheme of a supersonic expansion through a small nozzle. Zone of action (blue) and zone of silence (light blue) together form the Mach cone where the gas can reach Mach numbers much greater than one. At the borders a shock system (green) forms where the Mach number drops below one and the expansion no longer remains undisturbed. The border where  $M=1$  is referred to as Mach disc and is further perturbed by a skimmer inserted right into the zone of silence. Image taken from [11].

For a constant molar number and a transition from a high-pressure region with the pressure  $p_0$  to a low-pressure region  $p_1$  the equation can be written as

$$p_0^{1-\gamma} T_0^\gamma = p_1^{1-\gamma} T_1^\gamma \quad (5)$$

which can be simplified to

$$\left(\frac{T_0}{T_1}\right)^\gamma = \left(\frac{p_1}{p_0}\right)^{1-\gamma} \quad (6)$$

and finally to

$$\frac{T_0}{T_1} = \left(\frac{p_1}{p_0}\right)^{\frac{1-\gamma}{\gamma}} \quad (7)$$

which shows that a reversible, adiabatic process is directly linked to a change in temperature [15]. As gas flow always occurs from a high-pressure region to a low-pressure region in a nozzle, a supersonic expansion leads to a drop in temperature. This temperature drop leads to a decrease in the specific enthalpy  $H$  of the gas which is linked to the temperature

by

$$H = c_p T. \quad (8)$$

The Bernoulli equation for real gases on an isentropic streamline is given by

$$H + \frac{v^2}{2} + \Psi = \text{const} \quad (9)$$

with  $v$  as the velocity and  $\Psi$  as the force potential of the gas, usually the gravitational potential [16]. As such,  $\Psi$  is negligibly small for a gas moving at high speeds and thus can be omitted, leaving a simple relation between temperature and particle velocity:

$$c_p T + \frac{v^2}{2} = \text{const}. \quad (10)$$

Equation 10 shows that a supersonic expansion through a nozzle leads to a temperature drop which is directly linked to a velocity increase of the gas thus reaching velocities of several Mach numbers while undergoing a significant reduction in temperature.

### 3.2.2 Electrical discharges

The mountable discharge nozzle is built after a design by the Willitsch group from the University of Basel[17]. It is a DC discharge source with two electrodes which directly come in contact with the carrier gas to create a discharge that breaks the molecules apart with the goal to form new molecules. The setup of the nozzle is shown in Figure 2 and will be explained further in the experimental chapter.

Electrical discharges occur when an electric field ionizes a medium, allowing current to flow through. They are present in natural phenomena like lightning strikes or technological applications like welding or gas discharge lamps. When a voltage is applied between two electrodes it creates an electric field which ionizes the medium, often gas, causing an electron avalanche that strips electrons off their molecules. That mechanism is demonstrated in Figure 4. The free electrons then collide with other gas molecules while transferring energy and ionizing them. When the molecule relaxes it emits photons which can be visible as glow. That phenomenon is used in gas discharge lamps with gases like neon or sodium vapor. In this experiment, the goal is to use such an electrical discharge to excite the molecules high enough to break their bonds and cause them to react and form new molecules.

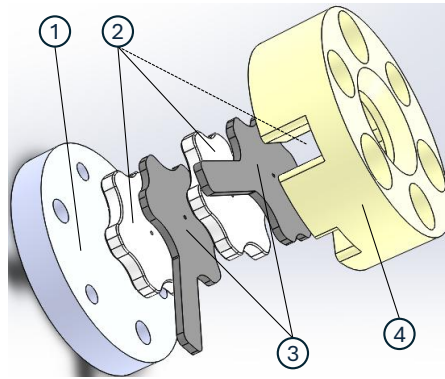


Figure 2: Exploded view of the mountable discharge nozzle. On top of the stainless steel backing plate (1) a stack of 3 MACOR plates (2), each measuring 2 mm in width, with stainless steel electrodes (3), each measuring 1 mm in width, in between. The third MACOR plate is hidden inside the teflon holder (4) which keeps the stack in place. Inside the stack there is a hole measuring  $0.5 \mu\text{m}$  in diameter where the gas can flow through. The  $45^\circ$  cone with a depth of 4 mm is not shown here.

An electrical discharge is dependent on several parameters, including the pressure of the medium, the type of gas, the applied voltage, and the geometry of the electrodes [18]. It is most thoroughly investigated for gas filled tubes like gas discharge lamps. The formation of a discharge results in the observation of multiple distinct regions whose sizes are determined by the aforementioned factors. These regions are shown in Figure 3. Near the cathode, where the electrons are emitted, the Aston dark space (Aston DS) is formed. In this region, the electron energy is insufficient to ionize or excite the gas. It can be identified as a thin dark layer around the cathode which borders the a cathode glow layer where the electrons have accumulated sufficient energy from the electric field to excite the gas. When the excited gas relaxes to its ground state, photons are emitted which, depending on the wavelength, can be observed as a glowing layer near the cathode. There can be more than one cathode glow layer. Next to the cathode layer, there is a dark space known as cathode dark space (cathode DS), Crooke or Hittorf dark space. With increasing energy of the electrons, the gas tends to be ionized more frequently, leading to the formation of ion and electron pairs. Due to the strong electric field, ions and electrons are separated and cannot recombine directly, resulting in a multiplication of charges in that region but no light emission. The emitted electrons from this region tend to be slower than the electrons from the cathode, and thus are able to recombine with positive ions headed towards the cathode more easily. This recombination process leads to the emission of light, referred to as the negative glow region. The continuous processes of ionization and

recombination lead to the gradual loss of energy by the electrons, to the extent that they are no longer capable of ionizing or exciting the gas. This results in the formation of the Faraday dark space (Faraday DS). The following positive column typically takes up most of the space within the discharge tube characterized by a decrease in the number of ions and an increase in the number of electrons due to previous ionization processes. That results in electrons exciting the gas and leading to photon emission. Near the anode, ions are repelled, while electrons are pulled out from the positive column, creating a strongly negative space charge and also increasing the electric field. The increased electric field leads to the anode glow, while the reduced electron density surrounding the anode forms the anode dark space (anode DS).

For a conventional low-pressure glow discharge tube, typical gas pressures vary from  $4 \cdot 10^{-2}$  mbar to 40 mbar, with voltages between 100 and 1000 V [18]. However, as the discharge nozzle shape in use is conical, parameters and the shape of the glow discharge may change drastically.

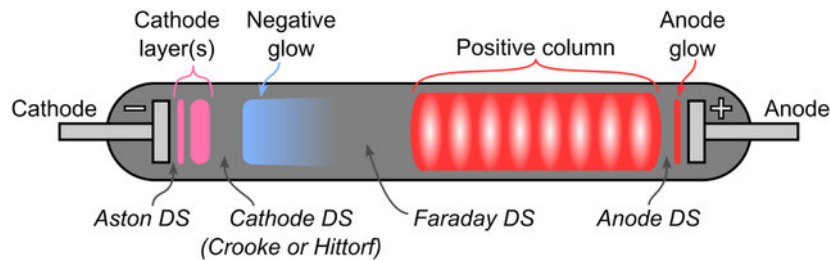


Figure 3: Formation of different regions during a discharge in a gas-filled discharge tube. Dark spaces are abbreviated by DS. Image taken from [19].

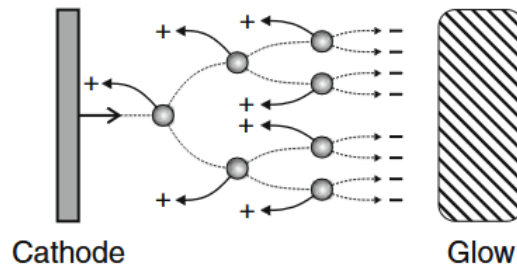


Figure 4: A single electron traveling from the cathode towards the anode can generate an electron avalanche while causing cations to move towards the cathode [20].

### 3.3 Molecular spectroscopy

To understand the REMPI technique, it is essential to take a look into molecular theory. This chapter aims to give a brief overview into the topic and is mostly based upon Peter Bernath's textbook Spectra of Atoms and Molecules [21] where a more comprehensive understanding of the topic is provided. Both electrons and nuclei contribute to the total energy of a molecule. The Born-Oppenheimer approximation states that electronic motion occurs on a faster time scale than nuclear motion. Therefore electrons move in a quasi-static potential of the nuclei allowing for a separation of the energy into an electronic and a nuclear part

$$E = E_{el} + E_{nuc} \quad (11)$$

The nuclear contribution can then be further separated into a vibrational, and a rotational energy contribution. When using an accelerated coordinate system, a separation into vibrational and rotational contributions is not exact due to the Coriolis coupling of vibrational and rotational motion, which introduces mixing of their wavefunctions. However, for low-excited vibrational modes, this model has proven successful, leading to the following expression:

$$E = E_{el} + E_{vib} + E_{rot} \quad (12)$$

with

$$E_{el} \gg E_{vib} \gg E_{rot} \quad (13)$$

Typically, rotational energy contributions are in the microwave region, vibrational energies are in the infrared region, and electronic energies are in the optical and UV regions.

#### 3.3.1 Rotational spectroscopy

Molecules have a part of their energy stored as rotational energy as described above. A suitable model for the description of the rotational motion can be that of the rigid rotor. In this classical approach, an extended object has an angular velocity  $\omega$  and an angular momentum  $L$  that point out of the plane of rotation. For a rotating object  $\omega$  and  $L$  do not need to point in the same direction with is mathematically described by

$$\vec{L} = I\vec{\omega} \quad (14)$$

where  $I$  denotes the three-dimensional moment of inertia tensor in classical mechanics. It can be written explicitly as

$$\begin{pmatrix} L_x L_y L_z \end{pmatrix} = \begin{pmatrix} I_{xx} & I_{xy} & I_{xz} \\ I_{xy} & I_{yy} & I_{yz} \\ I_{xz} & I_{yz} & I_{zz} \end{pmatrix} \begin{pmatrix} \omega_x \\ \omega_y \\ \omega_z \end{pmatrix}. \quad (15)$$

As  $I$  is a symmetric tensor, it can be diagonalized with all non-diagonal elements being zero. The diagonal elements represent the eigenvalues of  $I$  in the principal axis system of the molecule. In this system, the axes are chosen so that the z-axis has the highest order of rotational symmetry.

$$\begin{pmatrix} L_x L_y L_z \end{pmatrix} = \begin{pmatrix} I_x & 0 & 0 \\ 0 & I_y & 0 \\ 0 & 0 & I_z \end{pmatrix} \begin{pmatrix} \omega_x \\ \omega_y \\ \omega_z \end{pmatrix} \quad (16)$$

Based on the magnitude of the moments of inertia  $I_x$ ,  $I_y$  and  $I_z$  the axes are labeled  $a$ ,  $b$  and  $c$  so that

$$I_A \leq I_B \leq I_C. \quad (17)$$

This labeling scheme then allows for a classification of molecules according to their moments of inertia:

1. Linear molecules:  $I_A = 0, I_B = I_C$  (e.g. HF, CO<sub>2</sub>, C<sub>2</sub>H<sub>2</sub>)
2. Spherical tops:  $I_A = I_B = I_C$  (e.g. CH<sub>4</sub>, SF<sub>6</sub>)
3. Oblate symmetric tops:  $I_A = I_B < I_C$  (e.g. NH<sub>3</sub>, C<sub>6</sub>H<sub>6</sub>)
4. Prolate symmetric tops:  $I_A < I_B = I_C$  (e.g. CH<sub>3</sub>F)
5. Asymmetric tops:  $I_A < I_B < I_C$  (e.g. H<sub>2</sub>O)

In the most generalized case, the asymmetric top, the classical energy is given by

$$E = \frac{J_a^2}{2I_A} + \frac{J_b^2}{2I_B} + \frac{J_c^2}{2I_C} \quad (18)$$

which leads to the rotational Hamiltonian operator of a rigid rotor in a field-free space

$$\hat{H} = \frac{\hat{J}_a^2}{2I_A} + \frac{\hat{J}_b^2}{2I_B} + \frac{\hat{J}_c^2}{2I_C}. \quad (19)$$

$J_i$  represent the total angular momentum with respect to their axis, while  $\hat{J}_i$  represent their corresponding angular momentum operators. The resulting Schrödinger equation  $\hat{H}\psi = E\psi$  has no general analytic solution but simplifies for the cases shown above. In the case of a linear molecule with  $I_A = 0, I_B = I_C = I$ , the equation can be solved to yield the energy eigenvalues  $F(J)$

$$F(J) = BJ(J+1) \quad (20)$$

with the rotational constant

$$B = \frac{\hbar^2}{2I}. \quad (21)$$

As molecules are no rigid rotors but instead have a centrifugal force exerted on them, higher order correction terms can be introduced to account for the bond stretching between two atoms.

$$F(J) = BJ(J+1) - D(J(J+1))^2 \quad (22)$$

with  $D$  as the centrifugal distortion constant. Centrifugal distortion increases the internuclear distance  $r$ , therefore decreasing the effective rotational constant.

Both vibrational and electronic state have an influence on the rotational constant, so that every vibronic state has its own rotational constant. A vibronic (vibrational-electronic) state can have theoretically infinite rotational levels with rotational quantum numbers  $J = 0, 1, 2, \dots$  whose distribution is dependent on the temperature. In an unperturbed case, the rotational levels of symmetric and linear molecules each have a distance of  $2B$ , which decreases when a centrifugal distortion is introduced. Therefore subsequent rotational levels at higher  $J$  have a lower energy difference. Acetylene has a rotational constant of  $1.176 \text{ cm}^{-1}$  in its vibronic ground state [22], so a line distance of around  $2.3 \text{ cm}^{-1}$  can be expected.

### 3.3.2 Vibrational spectroscopy

In addition to the rotational energy, molecules have a part of their energy stored as vibrational energy. A molecule with  $N$  atoms can vibrate in  $3N - 6$  (5 for linear molecules) vibrational modes  $\nu_i$ . A diatomic molecule with a bond length  $r$  can be described by a Morse potential with an equilibrium distance  $r_e$ . Solving the Schrödinger equation yields the eigenvalues

$$E = \omega_e \left( \nu + \frac{1}{2} \right) - \omega_e \chi_e \left( \nu + \frac{1}{2} \right)^2 + B_e J(J+1) - D_e (J(J+1))^2 - \alpha_e \left( \nu + \frac{1}{2} \right) J(J+1). \quad (23)$$

with  $\nu$  as the vibrational quantum number,  $J$  as the rotational quantum number, and  $\chi_e$  as the anharmonicity constant, while  $\omega_e$ , and  $\alpha_e$  are described in [21] more thoroughly. While the first two terms in Equation 23 describe the vibrational levels only, the third and fourth terms resemble those from the rotor described in Equation 22. The fifth term is an interaction term of vibrational and rotational levels. When looking at the vibrational levels only, the three last terms can be omitted, leaving only the two terms

$$E = \omega_e \left( \nu + \frac{1}{2} \right) - \omega_e \chi_e \left( \nu + \frac{1}{2} \right)^2. \quad (24)$$

This equation shows, that for increasing vibrational quantum numbers  $\nu$ , the second term including the anharmonicity constant becomes more important thus reducing the energy distance between higher vibrational levels. Vibrational transitions follow the selection rule  $\Delta\nu = \pm 1, \pm 2, \pm 3, \dots$ , where the  $\nu = 1 \leftarrow 0$  is commonly referred to as *fundamental* and higher transitions like  $\nu = 2 \leftarrow 0$ ,  $\nu = 3 \leftarrow 0$ , ... as first, second, ... overtones. Typically, fundamental transitions have a higher intensity than overtone transitions.

Acetylene ( $C_2H_2$ ) is a linear hydrocarbon which consists of two carbon and two hydrogen atoms where the two carbon atoms are connected by a triple bond. According to  $3N - 5$  for linear molecules, acetylene has 7 vibrational modes. The bending modes  $\nu_4$  and  $\nu_5$  are doubly degenerate each due to another equivalent mode with the same frequency. An overview of the vibrational modes of acetylene is given in Table 1.

Table 1: Vibrational modes for acetylene in its electronic ground state [23].

Vibrational mode	Type	Frequency
$\nu_1$	Symmetric C-H stretch	$3372.84 \text{ cm}^{-1}$
$\nu_2$	Symmetric $C\equiv C$ stretch	$1974.35 \text{ cm}^{-1}$
$\nu_3$	Asymmetric C-H stretch	$3294.85 \text{ cm}^{-1}$
$\nu_4$	Symmetric bend	$612.86 \text{ cm}^{-1}$
$\nu_5$	Asymmetric bend	$730.33 \text{ cm}^{-1}$

### 3.3.3 Electronic spectroscopy

Electronic transitions refer to the movement of electrons between different energy levels in a molecule when they absorb or emit a photon. Transitions between these energy levels usually lie in the optical and ultraviolet region, each forming an orbital which describes the wavefunction of the electronic state. The sum of all orbitals in an atom or molecule defines their electronic configuration which is unique for all atoms and molecules. An electronic state incorporates vibrational energy levels which then incorporate rotational energy levels itself, leading to complex band structures in a spectrum. Again, the electronic states of a diatomic molecule can be described with Morse potentials with an internuclear distance  $r$  and an equilibrium distance  $r_e$ . For each electronic state the equilibrium distance varies which heavily influences the transition probability between two electronic states. Due to the Born-Oppenheimer approximation, it is assumed that the internuclear distance remains unchanged during an electronic transition. Consequently, transitions between states with different equilibrium distances become less likely for a low  $\Delta v$ , but instead increases the probability of transitions into highly vibrationally excited states, which is further addressed by the Franck-Condon principle. It describes the intensities of vibronic (electronic and vibrational) transitions from an initial state  $\psi''$  to a final state  $\psi'$ . The electronic transition dipole moment  $R_e(r)$  of such a transition is given by

$$R_e(r) = \langle \psi'_{el} | \mu | \psi''_{el} \rangle \quad (25)$$

with the molecular dipole operator  $\mu$  [21]. After expanding  $R_e(r)$  in a Taylor series with the equilibrium distance  $r_e$  as a value for  $r$ , the transition dipole moment  $M_{e\nu}$ , which includes both the electronic and vibrational transition into an electronic and a vibrational part can be written as follows:

$$M_{e\nu} = R_e(r_e) \langle \nu' | \nu'' \rangle. \quad (26)$$

Here, the transition dipole moment can be separated into a product of an electronic and a vibrational part. The intensity  $I$  of a vibronic transition is proportional to the squared transition moment

$$I \propto |R_e|^2 \cdot |\langle \nu' | \nu'' \rangle|^2 \quad (27)$$

with  $|\langle \nu' | \nu'' \rangle|^2$  as the *Franck-Condon factor* which determines the intensity distribution among the vibrational bands and  $|R_e|^2$ , a measure of the intrinsic strength of an electronic transition. While a transition between two electronic states with similar  $r_e$  is often favored

for  $v' = 0 \leftarrow v'' = 0$  due to a good overlap of the wavefunctions, transitions between states with different  $r_e$  may be favored for higher vibrational excitation in the final state or even be unfavored at all.

Electronic states in a molecule are generally labeled similarly to atoms and are referred to as molecular term symbols. Their general form is

$$^{2S+1}\Lambda_{g/u}^{\pm} \quad (28)$$

with  $S$  as the total spin quantum number,  $\Lambda$  as the projection of the total electronic angular momentum  $L$  on the molecular axis,  $\pm$  indicating reflection symmetry for  $\Sigma(\Lambda = 0)$  states, and  $g/u$  indicating the symmetry with respect to inversion for centrosymmetric molecules. In linear molecules, states with higher  $\Lambda$  are labeled with  $\Pi(\Lambda = 1)$ ,  $\Delta(\Lambda = 2)$ ,  $\Phi(\Lambda = 3)$  etc., while nonlinear molecules often include the irreducible representations of their point group. Molecular term symbols describe electronic configurations and are therefore not unique to a single electronic state. Thus, they can occur in different electronic states which are often labeled  $X$  for the ground state and  $A, B, C$ , etc. for first, second, third, etc. excited states.  $\tilde{X}, \tilde{A}, \tilde{B}, \tilde{C}$  are often used when vibrational states are taken into account as well. Other notations include ordering the states with  $X$  as the ground state and using 1, 2, 3 etc. for excited states, or using the molecular orbital notation 1s, 2s, 2p, etc.

In the case of acetylene, the ground state is labeled as a  $\tilde{X}^1\Sigma_g^+$  state. From the transition moment between two states a set of selection rules can be derived to describe whether such a transition is allowed, which is determined by factors like spin conservation or symmetry. The selection rules for a ro-vibronic transition are [24]:

$$J = 0, \pm 1 \quad (29)$$

$$\Delta\Lambda = \pm 1$$

$$\Delta S = 0$$

except for transitions from  $J=0$  to  $J=0$  which are forbidden. Note, that these selection rules are for transitions where only one photon is absorbed or emitted. For two- or more photons being absorbed at the same time, other selection rules apply, which may allow different transitions and are often relevant for REMPI processes which will be explained further in the next chapter.

### 3.4 Resonance-enhanced multi-photon ionization

Resonance-enhanced multi-photon ionization (REMPI) is a soft ionization method which incorporates the absorption of at least two photons to ionize a molecule. Usually, the absorption of multiple photons simultaneously occurs with a significantly lower probability than the absorption of a single photon. As the ionization energy for most molecules lies fairly high, radiation in the vacuum ultraviolet (VUV) range has to be used. As this radiation is typically difficult to handle outside of a vacuum due to absorption, the REMPI technique enables the use of radiation which is more accessible and easier to handle. The main drawback is the lower probability of absorbing multiple photons simultaneously. To tackle this problem, the absorption can be resonance-enhanced by addressing electronic states in the molecule. In a regular two-photon ionization (2PI) setting, a molecule would absorb two photons simultaneously to reach the ionization energy. A molecule in a 1+1 REMPI setting would instead absorb one photon exciting the molecule and afterwards absorb a second photon, increasing the probability to reach the ionization threshold if there is a proper electronic intermediate state. Other REMPI schemes are possible, often described as  $(n+m)$ -REMPI schemes, where  $n$  denotes the amount of resonant photons and  $m$  denotes the amount of non-resonant photons, e.g. 2+1, 3+1, or 2+2-REMPI schemes. The photons do not have to be of the same wavelength. Figure 5 illustrates some MPI and REMPI schemes for a hypothetical molecule. Note, that these processes do not necessarily have to start from the ground state but can start from higher excited states, e.g. vibrationally, as well. Due to its ability to selectively ionize, REMPI can be used spectroscopically providing spectral information about specific molecules.

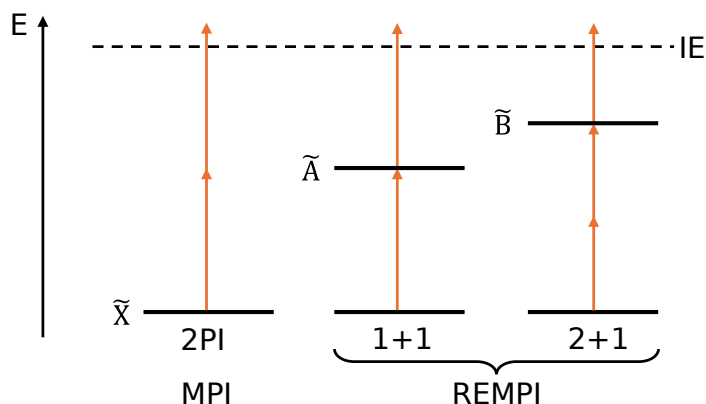


Figure 5: Multi-photon ionization (MPI) and resonance-enhanced multi-photon ionization (REMPI) schemes showing two-photon ionization (2PI) and resonant 1+1 and 2+1 REMPI schemes for a hypothetical molecule.  $\tilde{X}$  denotes the electronic ground state while  $\tilde{A}$  and  $\tilde{B}$  denote electronic excited states. The first numbers of 1+1 and 2+1 denote the amount of photons needed to excite the molecule to a higher electronic state while the second number denotes the amount of photons needed to reach the ionization energy (IE).

### 3.5 Mass spectrometry

The history of mass spectroscopy began in the early 20th century when Thomson [25] did his experiments on *cathode rays*. Building upon the contributions of Goldstein who discovered *Kanalstrahlen* in perforated cathodes in 1886 [26], and Wien, who discovered their properties as positively charged ions in 1898 [27], Thomson discovered the existence of Ne-20 and Ne-22 by discharging the sample in a discharge tube and subsequently passing it through an electric and magnetic field. The resulting trajectory depends on the charge-to-mass ratio  $q/m$  which could be measured by using a photographic plate. Subsequently, in 1918 and 1919, Dempster and Aston independently constructed prototypes of the first modern mass spectrometers, thereby enabling the further identification of various isotopes [28][29]. The first time-of-flight mass spectrometer was constructed in 1948 by Cameron and Eggers and optimized by Wiley and McLaren in 1955 [30][31]. Other notable developments in this field include the use of quadrupoles by Paul in 1953, the use of refletrons by Mamyrin in 1977 and the development of the orbitrap mass spectrometer by Makarov in 1999 [32][33].

Nowadays, mass spectrometry boasts a range of applications as an analytical technique in scenarios where the composition of a sample needs to be determined by separation of the contents masses. Given its capacity of measuring the  $q/m$  ratio alone, particles have to be ionized in order to be detected. This can be accomplished through various techniques

which are often categorized into hard and soft ionization techniques.

Hard ionization techniques like electron impact ionization (EI) usually transmit lots of energy (usually around 70 eV) into the molecule which leads to high residual energy further leading to large degrees of fragmentation to remove the excess energy and stabilize the remnants of the molecule. Usually this fragmentation leads to lower  $m/z$  values than the parent molecules. Soft ionization techniques like electrospray ionization (ESI), field ionization (FI) or REMPI transmit less energy into the molecule and therefore lead to less fragmentation. Depending on the technique, multi-ionization where the molecule is doubly, triply or higher charged can occur. As a soft ionization technique, REMPI is used as ionization method in conjunction with a Wiley-McLaren time-of-flight mass spectrometer as detection method. The low degrees of fragmentation and single-ionization that REMPI has, make REMPI an ideal choice for mass spectroscopy while providing spectral selectivity to detect specific molecules in a mixture.

The Wiley-McLaren time-of-flight mass spectrometer, is a type of mass spectrometer which enabled high-resolution measurements of ion masses through precise time-of-flight analysis. A conventional time-of-flight spectrometer where ions are accelerated by an electrical field and pass a field-free drift tube before hitting a detector suffers from broadening of mass signals due to different initial ion velocities. Here, only a repelling plate and a grounded plate are used to create the electrical field. Singly ionized particles receive the same energy in the electric field but have different velocities according to

$$E_{kin} = \frac{1}{2} \cdot m \cdot v^2 = q \cdot U_B \quad (30)$$

$$v = \sqrt{\frac{2 \cdot q \cdot U_B}{m}}. \quad (31)$$

Including the length of the drift tube leads to an expression for the time-of-flight depending on the drift tube length  $s$ , ion mass  $m$ , ion charge  $q$ , and acceleration voltage  $U_B$

$$t = s \cdot \sqrt{\frac{m}{2 \cdot q \cdot U_B}}. \quad (32)$$

Equation 32 shows that the time-of-flight is directly proportional to  $\sqrt{m}$  which results in decreased distances in time between adjacent masses for increasing masses. This eventually leads to the overlap of adjacent mass peaks. In theory, if all ions were formed in a plane parallel to the electrodes and had zero initial velocity parallel to the electric field, the time-of-flight would be equal for all ions with equal  $m/q$ . This would lead to a perfect

separation of peaks, limited only by detection equipment. However, in practice, the ions are formed in the space between the electrodes and possess an initial velocity component that may even be oriented anti-parallel to the electric field. This initial velocity distribution, in conjunction with the spatial offset, results in a significant broadening of mass peaks, consequently leading to reduced resolution for higher masses.

The Wiley-McLaren time-of-flight mass spectrometer addresses this issue by incorporating another accelerating stage in between the repelling and the grounded electrodes as illustrated in Figure 6. It shows the spectrometer setup with the additional electrode designated as the *extractor* electrode. Similar to the basic time-of-flight setup, extractor and grounded electrode each contain a large aperture where the ions can traverse. These ions then fly through the field-free drift tube until they hit a detector. That detector is capable of measuring the time-of-flight of the particles from which the mass-to-charge ratio can be derived. Being a soft ionization method which creates exclusively singly charged particles, REMPI enables a distinct mass to be detected without influences from higher charged particles.

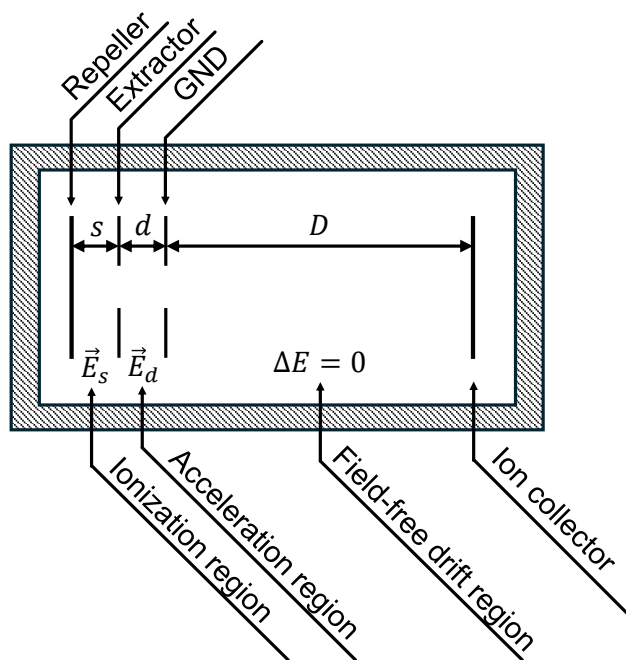


Figure 6: Modified schematic representation of the Wiley-McLaren time-of-flight mass spectrometer (based on [31], own illustration).  $\vec{E}_s$  and  $\vec{E}_d$  denote the electric fields in the ionization and acceleration region with their corresponding distances  $s$  and  $d$  respectively. The field-free drift region with length  $D$  after the grounded electrode is terminated with an ion collector.

Depending on repeller and extractor voltages and the distances between the electrodes, electric fields  $\vec{E}_s$  and  $\vec{E}_d$  are formed in the ionization region and acceleration region respectively. This two-staged setup allows for an improvement of space resolution and energy resolution, the former being related to the initial position of the ion and the latter being related to the initial energy of the ion.

An ion whose initial position is closer to the detector acquires less energy and may be overtaken by other ions whose initial position is further away. Consequently, that leads to a signal broadening. Wiley and McLaren could show that for a fixed geometry with constant acceleration distance  $d$ , drift length  $D$  and average initial position  $s_0$ , the space focus is determined by the ratio of  $E_d/E_s$ . Thus, it is possible to find a space resolution optimum by simply adjusting the applied repeller and extractor voltages.

### 3.6 Mass calibration

The data acquisition is done in a step-scan measurement, which will be explained in Chapter 4.3 more in detail, and generates timetraces for each wavelength within the measured range. If these are summed up, an uncalibrated spectrum containing all flight times over the course of the measured range is created. The recorded flight times are dependent on several experimental parameters like repeller and extractor voltage, etc.. Therefore a calibration is needed, where these parameters are kept constant to safely draw conclusions from the measured flight times. Equation 32 is used in a slightly modified form to create a fit between mass and flight time using Python allowing them to be converted into each other freely. The datasets used for the fit originate from previous experiments with equal experimental parameters.

## 4 Experimental

### 4.1 Experimental setup

The experimental setup is a four-stage vacuum chamber, comprising an expansion chamber, a differential stage, the interaction chamber and a beam dump.

#### 4.1.1 Expansion

Inside the expansion chamber an Even-Lavie-valve is mounted horizontally on three holders which are connected to an UHV precision manipulator. This manipulator allows for a precise adjustment of the valve in all three spatial dimensions. A CF25 stainless steel gas feedthrough flange is attached to the chamber and connects the external gas supply with the valve via a thin coiled stainless steel pipe. The Even-Lavie valve is equipped with a discharge nozzle as illustrated in Figure 7 and will be explained more in Chapter 4.1.3. The supersonic jet ejected by the valve is skimmed by a nickel skimmer with an orifice of 4 mm. Afterwards, the skimmed jet (now referred to as molecular beam) propagates through the first differential chamber which is separated from the second differential chamber by another copper skimmer with an orifice of 3 mm. These differential stages improve the quality of the beam and allow additional instruments to be installed for future experiments. Two turbomolecular pumps are used to pump the expansion chamber down to around  $10^{-9}$  mbar in idle and  $10^{-6}$  mbar under load. Under load, which means when the nozzle is operating, the pressure usually reaches  $10^{-6}$  mbar to  $10^{-5}$  mbar. The two differential stages are pumped by one turbomolecular pump each.

#### 4.1.2 Interaction chamber

After the second differential stage, the beam enters the interaction chamber. It is equipped with two windows made from UV-enhanced fused silica on either side, through which the laser beam can cross the molecular beam perpendicularly. In the center of the chamber, three circular electrodes are mounted via Teflon mounts so that both the molecular beam and the laser beam can traverse between the two lowermost electrodes. The molecular beam is then directed onto a beam dump. In the interaction stage, the Wiley-McLaren mass spectrometer is located, where at the electrodes, from bottom to top, voltages of +2000 V, +1400 V and 0 V are applied as illustrated in Figure 7. The electrodes are spaced with a distance of 11 mm between repeller and extractor and 20 mm between extractor and

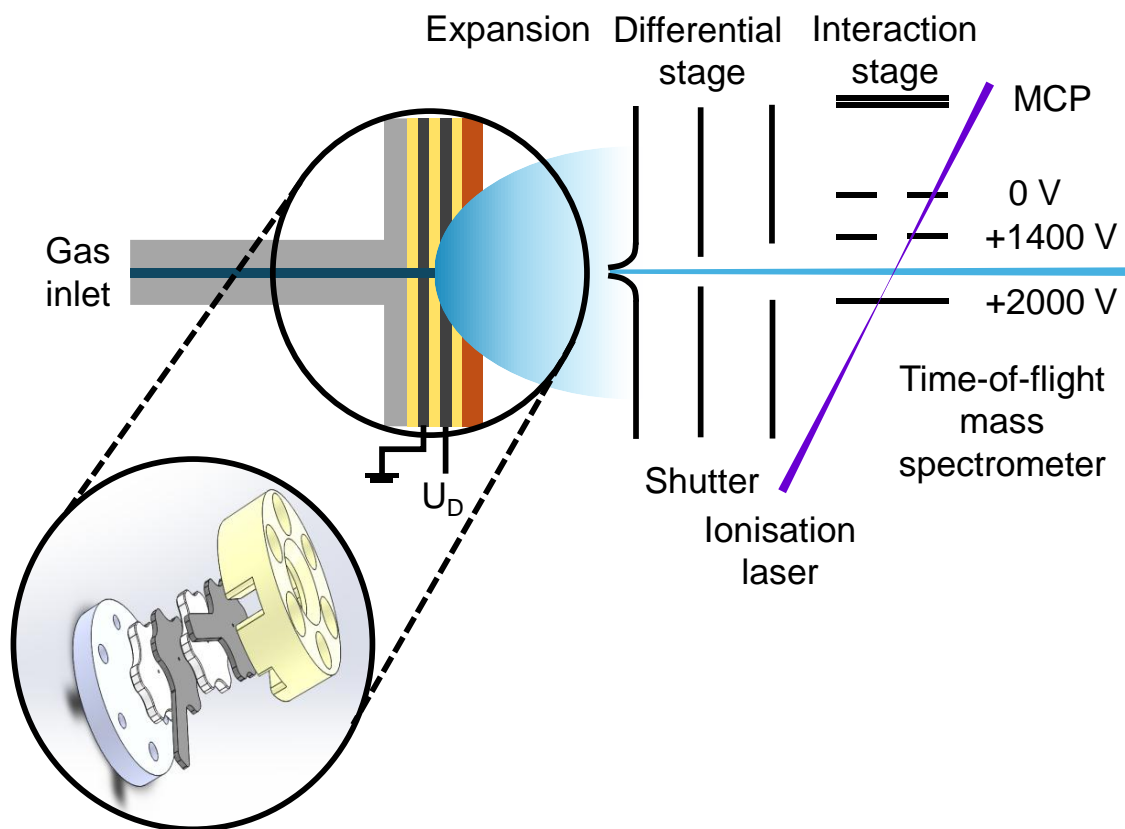


Figure 7: This schematic shows the experimental setup. The Even-Lavie valve on the left side (in gray) is mounted with a discharge nozzle (shown in the circle). It consists of two stainless steel electrodes (1mm width) separated by two MACOR insulating plates (2 mm width). Everything is held together by a teflon top which holds a third MACOR plate inside (2 mm width) and a stainless steel back plate.

ground. Above the electrodes a drift tube with a length of 10 cm connects the mass spectrometer with a V-stack of two micro-channel plates (MCP). The laser beam is focused onto the molecular beam by a convex lens with a focal length of 150 mm. When the molecular beam interacts with the ionization laser ions are produced and accelerated in the electric field. Positively charged ions are accelerated towards the MCP detector and can be measured there while negative particles like electrons are accelerated towards the repeller and are lost. An ion hitting the MCP detector triggers an electron cascade in its front plate which gets amplified by applying a voltage. Here, voltages of 1400-2000 V are applied depending on the target signal amplification.

### 4.1.3 The Even-Lavie valve

In order to create a molecular beam, a supersonic expansion in conjunction with a skimmer is needed as shown in Figure 1. A supersonic expansion can be achieved when a high-pressure gas enters a low-pressure region leading to both acceleration and cooling of the gas. The skimmer allows an extraction of a small portion of the expanding gas after which the . Supersonic expansions can be observed in nozzles, such as jet engines, or rocket propulsion. For this work the Even-Lavie valve by U. Even and N. Lavie is employed [34]. It is capable of producing pulses at up to 500 Hz with backing pressures up to 100 bar. Opening times can vary between 10 and 100  $\mu$ s according to the driver, however, the actual spatial of the gas pulse seemed to be longer throughout the experiment. Additionally, low backing pressures around 1 - 10 bar prevent the valve from opening longer than a certain threshold which increases with increasing backing pressure.

The valve cross section is shown in Figure 8. It is comprised of an (1) inlet, a thin-walled pressure vessel made from Inconel 625 (6) and an outlet (13). The inlet is a stainless steel tube which is connected to the pressure vessel via a pressure relief valve (2) which is sealed from the pressure vessel using a tightening spring (2) and a Kapton foil gasket (3). Inside the vessel there is a reciprocating plunger made from magnetic stainless steel (7) which is guided by two ruby ferrules (4, 10). A Kapton insulated copper coil (8), a magnetic shield (9) and a field concentrator (9) create a magnetic field in the vessel, which accelerates the plunger backwards and therefore opens the vessel to the outlet. In its initial state, a return spring made from Nimonic 19 alloy (5) holds the plunger in place and seals the vessel against the outlet. Another Kapton foil gasket (11) prevents leaking from the vessel. As the carrier gas only comes in contact with Inconel, stainless steel alloys and Kapton, a large variety of molecules can be used except for corrosives and amines which can wear down the Kapton gaskets. Under optimal conditions, the Even-Lavie valve allows helium to be cooled down to 10 mK and krypton or argon to be cooled down to 1 K.

The expansion nozzle can be replaced with a mountable discharge nozzle which is shown in Figure 7. As already mentioned, it has been adapted from the Willitsch group from the University of Basel as described by Straňák et al. [17]. The apparatus comprises two stainless steel electrodes, each measuring 1 mm in width separated by a MACOR plate, measuring 2 mm in width. Two additional MACOR plates insulate the electrodes from the stainless steel backing plate and the teflon top which hold everything together. A triggerable high voltage supply allows the front electrode to be charged with up to -1500 V

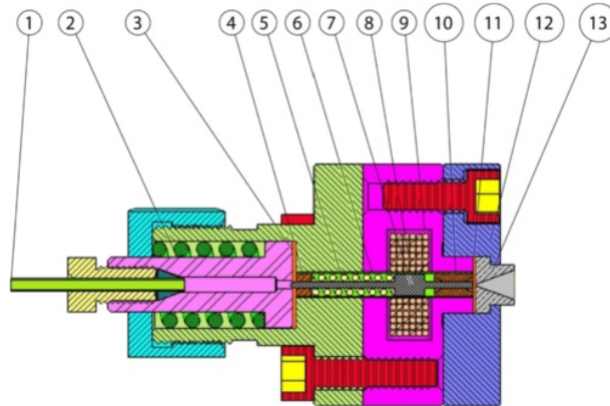


Figure 8: Cross section of the Even-Lavie valve by U. Even and N. Lavie [34]. At the back, there is a stainless steel gas inlet tube (1) which is connected to a tightening spring and pressure relief valve (2). It is sealed from the thin-walled pressure vessel (6) including the magnetic reciprocating plunger (7), the return spring (5), the ruby rear and front guiding ferrules (4, 10) via a Kapton foil gasket (3). Outside of the vessel, the Kapton insulated copper coil (8), magnetic shield, and field concentrator (9) are located. Another Kapton foil gasket seals the vessel from the expansion nozzle (13) which is fixed to the front via a stainless steel flange (12).

while the other electrode remains grounded. Triggering the voltage supply adequately, e.g. every second nozzle pulse, enables the discharge to alternate between pulses allowing on and off measurements. Within the electrodes and MACOR plates there is a hole with a diameter of 0.5 mm where the carrier gas passes through. This tube then opens into a cone with  $45^\circ$  opening angle and a depth of 4 mm.

## 4.2 Radiation source

The laser source used for all experiments conducted in this work is a customized *Tunable Wavelength Picosecond Laser* belonging to the PT403-SH/SF series, manufactured by EKSPLA. It features a tuning range from 210 to 2300 nm with typical pulse durations of 20 ps, a linewidth below  $9 \text{ cm}^{-1}$ , and a repetition rate of 100 Hz. The system is comprised of 3 different functional components, a pump laser, harmonics generators, and a tunable parametric stage. A diode-pumped, air-cooled, mode-locked Nd:YVO<sub>4</sub> laser of the *PL2210* series by EKSPLA serves as the pump laser which emits light at 1064 nm. The emitted light is then passed into a regenerative amplifier which is a monolithic machined cavity made from aluminum with a diode-pumped Nd:YAG rod protected by a Pockels cell. The beam is then amplified through stimulated emission until a threshold is reached and then directed to further stages. Inserting several different nonlinear crystals into the beam path enables the generation of frequency-doubled, tripled, quadrupled and quintupled outputs. The frequency tripled output of 355 nm is passed to the tunable parametric stage where the beam is split into two parts. The first part is directed to the optical parametric oscillator (OPO) stage where the beam passes through two OPO crystals. These OPO crystals generate a broadband, diverging *signal* and *idler* beam through superfluorescence which are reflected back into the same crystals. This backreflection occurs in conjunction with the pump beam, resulting in a reduction of divergence and spectral width. Subsequently, signal and idler beams are passed through a delay line to the optical parametric amplifier (OPA) stage. Here signal and idler beam reach the OPA stage exactly at the same time as the second 355 nm beam. The signal and idler beam seed the OPA crystals and are amplified by the 355 nm pump beam. After a single pass, the pump pulse is separated from the beam. A Rochon prism then separates signal and idler pulses. As signal and idler are limited to wavelength ranges of 410-710 nm and 710-2300 nm respectively, another stage is necessary to generate shorter wavelengths. For this purpose two type I BBO crystals are used. The first one generates the second harmonic from the signal beam and is limited to a range between 210 and 296 nm. The range between 296 nm and 410 nm is covered by the other BBO crystal which generates the sum frequency of the signal beam and the fundamental beam.

In this work, only the range from 210 to 280 nm was used with typical pulse energies of 3-15  $\mu\text{J}$ . Furthermore, it is known that the laser inherits a slight wavelength offset which has yet to be determined and is not considered in this work.

### 4.3 Data acquisition

To ensure that all components of the experiment are running correctly and coherently a pulse generator is employed. The device is manufactured by Quantum Composers Inc., it can maintain up to eight channels simultaneously and has a timing resolution of 250 ps. This allows for a precise synchronization of the laser, the valve, and the discharge nozzle. The adjustable delay times for each channel allow the discharge to be shifted to an earlier or later point in time during the expansion phase, or alternatively, to shift the laser pulse to probe different regions of the molecular beam. The internal clock of the pulse generator was set to 100 Hz for the UV-OPO and the nozzle trigger and to 50 Hz for the discharge trigger. This allows probing the molecular beam in both the on and off discharge stages, as well as the subtraction of recorded data during subsequent analysis.

Data are recorded using a software program developed in *LabView*. The software is connected to both the laser and the digitizer, which is responsible for reading out the voltage of the MCP output. The digitizer is triggered by an internal photodiode inside the laser which is in turn triggered by scattered laser light. Whenever a laser pulse is emitted from the laser, it triggers the photo diode which triggers the MCP and a raw time-of-flight spectrum is recorded. The software detects if the discharge was turned on or off and saves it. This process is repeated several, usually 64 unless stated otherwise, times for on and off measurements respectively and the raw spectra are averaged. Afterwards the laser is tuned to the next wavelength within the desired scanning range and the whole process is repeated again, often called a step-scan measurement.

## 5 Results and evaluation

In this section, the experimental data is presented and analysed. The goal of this work is to identify species formed in an acetylene discharge using REMPI. Thus, the evaluation methodology consists of the identification of these species, first by mass only and then by analyzing the UV-spectra the REMPI technique provides. This is done by evaluating the electronic transitions of the molecules and comparing them with existing data to ensure their presence in the molecular beam. After the electronic transitions are known, they can be used to determine relative yields while systematically varying the discharge conditions by the following parameters:

- Voltage: The voltage applied to the electrodes
- Backing pressure: The pressure the gas mixture has in the reservoir before entering the nozzle
- Nozzle opening time: The set time during which the nozzle is opened
- Discharge delay: The time between the discharge and the nozzle being triggered, can be either positive (discharge trigger comes after the nozzle trigger) or negative (discharge trigger comes before the nozzle trigger)
- Discharge pulse length: The duration after the discharge trigger where the set voltage is provided
- Nozzle delay: The time between the nozzle trigger and the laser trigger. As higher nozzle delays imply earlier interaction with the laser and vice versa, another metric was used instead, which uses an arbitrary but fixed time  $t_0 = 0\mu\text{s}$  where no signal from the pulse is visible.

These parameters were controlled via the quantum composer except for the voltage and the backing pressure, which were controlled via a HV source and a pressure gauge respectively. In this work, the experiment is limited to the presumably most important parameters being varied, namely backing pressure, nozzle opening time voltage, and nozzle delay. The discharge delay was kept at  $-150\mu\text{s}$  compared to the nozzle trigger for all measurements, ensuring that the voltage is provided at the electrodes when the nozzle opens. The discharge pulse length was kept at  $700\mu\text{s}$ .

## 5.1 Acetylene

For the acetylene discharge experiment, the Even-Lavie valve with the mounted discharge nozzle was used in the aforementioned vacuum chamber setup. Two measurements were performed with varying parameters to receive mass spectra. The first measurement was performed with 5 bar of 2% acetylene in helium in a range of 210-237 nm in steps of 0.01 nm where 64 averages were used to generate a spectrum for each step. The nozzle opening time was set to 40  $\mu$ s. Additionally, the discharge nozzle was set at 900 V and a duty cycle of 1:1 enabling a discharge-on-off measurement so the background could be subtracted from the spectrum during data analysis. The discharge-off spectra were subtracted from the discharge-on spectra and summed over all wavelengths, leaving only the discharge products. This method does not distinguish between resonant and non-resonant ionization and only shows the total signal intensity for each mass channel. The second measurement was performed at 10 bar of 0.5% acetylene in helium in a range of 210-280 nm in steps of 0.02 nm. Again, 64 averages were used here. The nozzle opening time was set to 28  $\mu$ s and the voltage was set to 1100 V. As the parameters differ a lot between the two measurements, their influence on certain mass channels will be discussed later in this work.

The mass spectra in Figure 9 and Figure 10 show that a large variety of species have been produced in the discharge with masses up to 102 u. As only acetylene and helium were involved as precursors it can safely be assumed that only hydrocarbons are formed in the discharge process. Comparing these two mass spectra shows that the peaks in both spectra appear grouped. Groups like (12, 13) u, (24, 25, 26) u, (36, 37, 38) u, (48, 49, 50) u (60, 61, 62, 63) u, (72, 73, 74, 75, 76) u, (84, 85, 86) u, (98, 99, 100, 102) u can be observed at varying intensities depending on the experimental parameters. Tables 2 and 3 present the relative intensities expressed as multiples of the standard deviation, denoted as  $\sigma$ , of the noise. Given the presence of an unequal number of data points in both measurements, this method allows at least some degree of comparability between the spectra. The standard deviation of the noise was determined by first identifying the intensity distribution of a large segment of the spectrum with no peaks present, subsequently fitting a normal distribution to it and finally extracting the standard deviation. Fitting a Voigt profile to each of the peaks in the mass spectrum allows the determination of the intensity of the respective mass channels which then can be expressed in multiples of  $\sigma$ . The signal-to-

noise ratio  $SNR$  is proportional to the amount of measurements  $N$ :

$$SNR \propto \sqrt{N} \quad (33)$$

As the first measurement consists of 2701 steps and the second consists of 3501 steps, a correction factor of  $\sqrt{\frac{3501}{2701}} \approx 1.14$  was applied. However, other factors like laser power or molecular electronic states further skew the comparability, but will be discussed later.

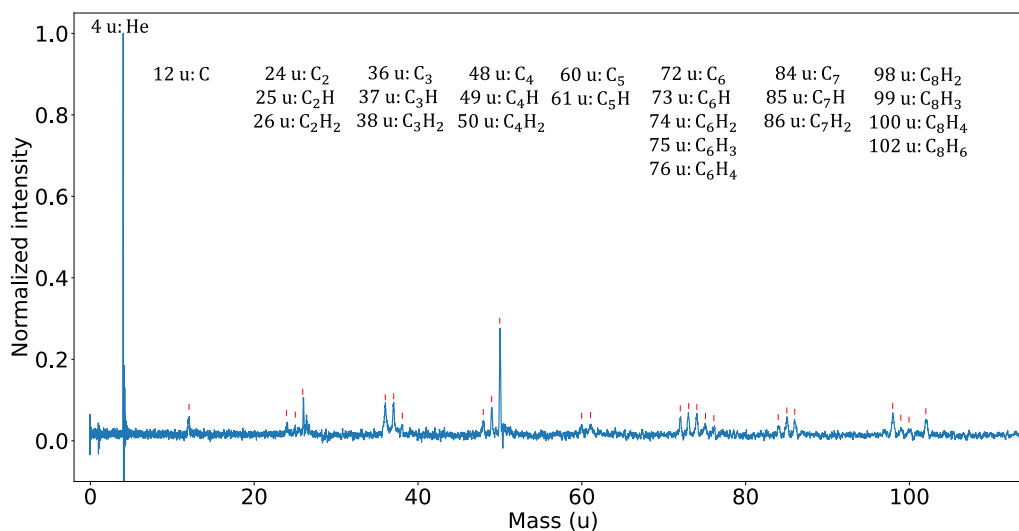


Figure 9: Mass spectrum of 2% acetylene in helium in a discharge with an opening time of  $40\mu\text{s}$ , 5 bar of backing pressure and a voltage of 900 V. The spectrum shown is a difference spectrum between discharge turned on and off, leaving only the masses produced by the discharge. Peaks are grouped into masses with equal amounts of carbon atoms and labeled with red lines. The intensity has been normalised to the helium peak.

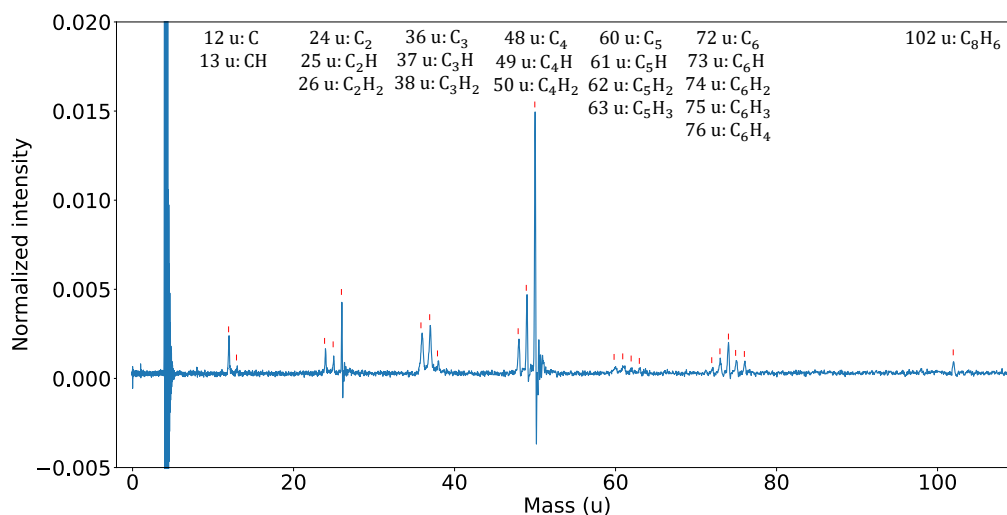


Figure 10: Mass spectrum of 0.5 % acetylene in helium in a discharge with an opening time of  $28\mu\text{s}$ , 10 bar of backing pressure and a discharge voltage of 1100 V. The spectrum shown is a difference spectrum between the discharge being turned on and off, leaving only the masses produced by the discharge. Peaks are grouped into masses with the same amount of carbon atoms and labeled with red lines. The intensity has been normalised to the helium peak which is cut out to enhance visibility of other peaks.

Table 2: Intensities for visible peaks in the mass spectrum shown in Figure 9. The intensity is given in multiples of the standard deviation of the background noise. Peaks with an intensity below  $3\sigma$  are ignored.

Mass	Intensity	Mass	Intensity	Mass	Intensity	Mass	Intensity
CH <sub>n</sub>		C <sub>3</sub> H <sub>n</sub>		C <sub>5</sub> H <sub>n</sub>		C <sub>7</sub> H <sub>n</sub>	
12 u	10	36 u	15	60 u	4	84 u	5
13 u	-	37 u	17	61 u	5	85 u	9
		38 u	6	62 u	-	86 u	8
				63 u	-		
C <sub>2</sub> H <sub>n</sub>		C <sub>4</sub> H <sub>n</sub>		C <sub>6</sub> H <sub>n</sub>		C <sub>8</sub> H <sub>n</sub>	
24 u	6	48 u	7	72 u	9	98 u	11
25 u	5	49 u	15	73 u	12	99 u	4
26 u	20	50 u	59	74 u	11	100 u	3
				75 u	5	102 u	9
				76 u	3		

Both spectra show a strong peak for the mass 50 u which appears to be the strongest hydrocarbon peak. Other notable peaks are 12 u, 26 u, 36 u, 37 u, 48 u, 49 u and 74 u. Thus, the C<sub>4</sub>H<sub>n</sub> group seems to be produced the most under the aforementioned conditions. Be-

Table 3: Intensities for visible peaks in the mass spectrum shown in Figure 10. The intensity is given in multiples of the standard deviation of the background noise. Peaks with an intensity below  $3\sigma$  are ignored. A correction factor of  $\sqrt{\frac{3501}{2701}} \approx 1.14$  was applied.

Mass	Intensity	Mass	Intensity	Mass	Intensity	Mass	Intensity
$\text{CH}_n$		$\text{C}_3\text{H}_n$		$\text{C}_5\text{H}_n$		$\text{C}_7\text{H}_n$	
12 u	12	36 u	13	60 u	-	84 u	-
13 u	-	37 u	16	61 u	-	85 u	-
		38 u	-	62 u	-	86 u	-
				63 u	-		
$\text{C}_2\text{H}_n$		$\text{C}_4\text{H}_n$		$\text{C}_6\text{H}_n$		$\text{C}_8\text{H}_n$	
24 u	8	48 u	11	72 u	-	98 u	-
25 u	5	49 u	27	73 u	4	99 u	-
26 u	25	50 u	90	74 u	11	100 u	-
				75 u	4	102 u	3
				76 u	3		

tween the two measurements, the  $\text{C}_{(1-4)}\text{H}_n$  groups have increased in intensity while the groups of  $\text{C}_{(5-8)}\text{H}_n$  have decreased. This suggests that lower densities of acetylene and lower voltages tend to produce more of the smaller hydrocarbon species. This may occur due to less carbon being available to form bigger species and less energy being transferred in the discharge to destroy bigger species. However, these may also be competing parameters, therefore the influence of backing pressure, nozzle opening time and voltage particularly on the mass 50 u yield will be illuminated further in the course of this work. From the recorded data it is possible to create UV-spectra of each mass channel by taking a single timetrace, calculating the area under the corresponding peak and plotting it against the wavelength. This was performed for all mass channels, though only 26 u and 50 u showed any spectral features. The spectrum for the 26 u mass channel was generated from the discharge-off measurement and is shown in Figure 11. The spectrum for the 50 u mass channel was generated by extracting a difference spectrum of discharge-on and discharge-off measurements and is shown in Figure 12.

Figure 11 shows the REMPI spectrum in the range of  $71700$  to  $84200\text{ cm}^{-1}$  with the range between  $76500$  and  $82000\text{ cm}^{-1}$  being cut out due to a lack of peaks. This was done to enhance the visibility of other peaks. The spectrum was recorded with a resolution of  $0.02\text{ nm}$  and a spectral width of  $<9\text{ cm}^{-1}$ . As the ionization threshold lies around  $91956\text{ cm}^{-1}$ , at least three photons are necessary to reach that energy essentially showing that a 2+1-REMPI process is required. Eight peaks are visible between  $72300\text{ cm}^{-1}$  and

76100 cm<sup>-1</sup>, one peak is visible at 82583 cm<sup>-1</sup>. A list of all peaks is shown in Table 4. Considering the temperature properties of a molecular beam after expansion ranging around several kelvin, it can be assumed that most if not all electronic transitions happen from the ground state  $\tilde{X}^1\Sigma_g^+$  denoted as  $\tilde{X}$  from now on. This will be further evaluated by comparing the signals with already published spectra. Errors given in parenthesis originate from the systematic error due to wavelength uncertainty from the laser (assumed to be  $\pm 4.5$  cm<sup>-1</sup> and doubled due to being a two-photon process) and the statistical error from the fit. The error from the laser offset is not included.

The first signal at  $(72320.3 \pm 9.2)$  cm<sup>-1</sup> is very weak and can be assigned to the triplet  $3p^3\Sigma_g^+$  state. [35] As the reference is given with  $(8.98 \pm 0.02)$  eV which, converted to wavenumbers, covers a range of 72267-72590 cm<sup>-1</sup> this assignment remains uncertain.

The second signal at  $(72764.9 \pm 9.2)$  cm<sup>-1</sup> is quite strong and can be assigned to the singlet  $3p^1\Delta_g^+$  state according to Tsuji et al. [36]. Between their observation of 72744.1 cm<sup>-1</sup> and this signal lies a deviation of around 20 cm<sup>-1</sup>.

Right next to this signal a smaller peak can be observed which blends into the previous. For this signal, no assignment could be found and needs more investigation.

The next signal is stronger and lies at  $(73988.2 \pm 9.3)$  cm<sup>-1</sup> and can be assigned to the  $3p^1\Delta_g 4^2$  state [36]. This notation denotes that the bending mode  $\nu_4$  in the  $3p^1\Delta_g$  state is excited with two quanta.

The next signal is the strongest within the measured range and lies at  $(74294.0 \pm 9.3)$  cm<sup>-1</sup>. It can be assigned to the  $3p^1\Sigma_g^+$  state and is not vibrationally excited [36]. Between the reference and the observed signal lies a difference of 15 cm<sup>-1</sup>.

A weaker signal follows at  $(74398.0 \pm 9.4)$  cm<sup>-1</sup> which can be assigned to the  $3p^1\Pi_g$  state [37]. For a two-photon process such a transition is forbidden due to selection rules, but can still be allowed, if a change in geometry is happening. In this case, the acetylene changes its geometry from a linear to a bent state, allowing the transition.

Afterwards, a smaller, broad signal comes at  $(74578.0 \pm 9.4)$  cm<sup>-1</sup> which can be assigned to the  $3p^1\Delta_g 2^1$  state [36]. Here, the symmetric C≡C stretching mode  $\nu_2$  in the  $3p^1\Delta_g$  state is excited with one quantum. Between the reference and the observation lies a difference of 24 cm<sup>-1</sup>.

Then a small signal at  $(75778.2 \pm 9.5)$  cm<sup>-1</sup> follows, which can be assigned to the  $3p^1\Delta_g 2^1 4^2$  state [36]. In this case,  $\nu_2$  and  $\nu_4$  of the  $3p^1\Delta_g$  state are excited with one and two quanta respectively. The difference between reference and observation is around 17 cm<sup>-1</sup>.

Another stronger signal lies at  $(76098.3 \pm 9.5)$  cm<sup>-1</sup> and can be assigned to the  $3p^1\Sigma_g^+ 2^1$  state [36]. Here, the  $\nu_2$  mode of the  $3p^1\Sigma_g^+$  state is excited with one quantum. The dif-

ference between reference and observation is around  $13 \text{ cm}^{-1}$ .

After a range with no signals, another small peak can be observed at  $(82581.1 \pm 10.1) \text{ cm}^{-1}$ . In contrast to the previous signals, this transition does not belong to the 3p-orbital but to the 4p-orbital, the  $4p^1\Delta_g$  state, instead [36]. The difference between reference and observation is around  $20 \text{ cm}^{-1}$ .

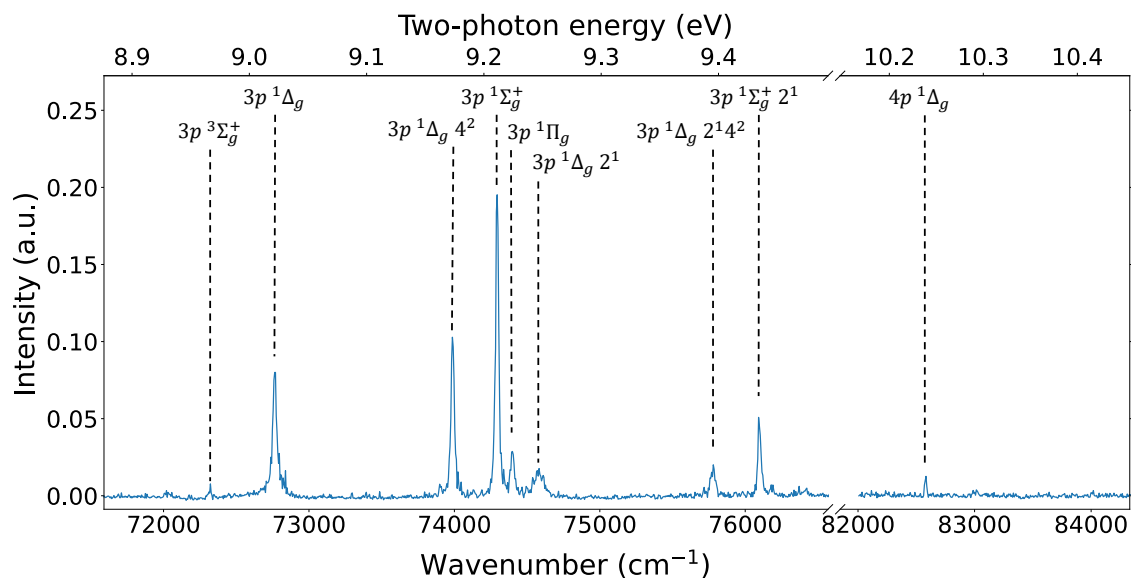


Figure 11: 2+1-REMPI spectrum of acetylene in the range of  $71700$  to  $84200 \text{ cm}^{-1}$ . Due to a lack of peaks the range between  $76500$  and  $82000$  has been cut out to enhance visibility of the other peaks. Labeled peaks are transitions from the ground state  $\tilde{X}^1\Sigma_g^+$  to the respective state.

Table 4: List of peaks shown in Figure 11 with their respective assignment.

Energy	Reference	Assignment
$(72320.3 \pm 9.2) \text{ cm}^{-1}$	$(8.98 \pm 0.02) \text{ eV}^a$	$3p^3\Sigma_g^+{}^a$
$(72764.9 \pm 9.2) \text{ cm}^{-1}$	$72744.1 \text{ cm}^{-1}{}^b$	$3p^1\Delta_g{}^b$
$(73988.2 \pm 9.3) \text{ cm}^{-1}$	$73969.3 \text{ cm}^{-1}{}^b$	$3p^1\Delta_g 4^2{}^b$
$(74294.0 \pm 9.3) \text{ cm}^{-1}$	$74279.0 \text{ cm}^{-1}{}^b$	$3p^1\Sigma_g^+{}^b$
$(74398.0 \pm 9.4) \text{ cm}^{-1}$	-	$3p^1\Pi_g{}^c$
$(74578.0 \pm 9.4) \text{ cm}^{-1}$	$74554 \text{ cm}^{-1}{}^b$	$3p^1\Delta_g 2^1{}^b$
$(75778.2 \pm 9.5) \text{ cm}^{-1}$	$75760.8 \text{ cm}^{-1}{}^b$	$3p^1\Delta_g 2^1 4^2{}^b$
$(76098.3 \pm 9.5) \text{ cm}^{-1}$	$76085.0 \text{ cm}^{-1}{}^b$	$3p^1\Sigma_g^+ 2^1{}^b$
$(82581.1 \pm 10.1) \text{ cm}^{-1}$	$82561.5 \text{ cm}^{-1}{}^b$	$4p^1\Delta_g{}^b$

<sup>a</sup>photoabsorption spectra [35]

<sup>b</sup>fluorescence excitation spectra [36]

<sup>c</sup>two-color double resonance spectra [37]

Comparing these signals with each other shows that several of them belong to the same electronic states  $3p^1\Delta_g$  and  $3p^1\Sigma_g^+$  respectively, though being excited to different vibrational levels. For the  $3p^1\Delta_g$  state a short vibrational progression of the  $\nu_2$  and  $\nu_4$  modes can be observed allowing the energy of these modes in that state to be estimated. The same can be performed for the  $\nu_2$  mode in the  $3p^1\Sigma_g^+$  state. The former yields an energy of  $1813 \text{ cm}^{-1}$  for the  $\nu_2$  and an energy of  $612 \text{ cm}^{-1}$  for the  $\nu_4$  mode while the latter yields an energy of  $1804 \text{ cm}^{-1}$  for the  $\nu_2$ . Comparing these with modes in the ground state [23], where the  $\nu_2$  mode has an energy of  $1974.35 \text{ cm}^{-1}$  and the  $\nu_4$  mode has an energy of  $612.86 \text{ cm}^{-1}$ , it can be observed that the  $\text{C}\equiv\text{C}$  stretching mode  $\nu_2$  has notably lower energy in these two excited states than in the ground state while the symmetric trans bending mode  $\nu_4$  almost did not change at all. A coupling between the  $\nu_4$  and the  $\nu_2$  can be observed as the distance between the  $3p^1\Delta_g 2^1$  and the  $3p^1\Delta_g 2^1 4^2$  states is  $1200 \text{ cm}^{-1}$ , a little less than twice the  $\nu_4$  energy in the ground state. However, the limited amount of visible transitions within these states does not allow further insight on the vibrational modes in these electronically excited states. Most importantly though, the spectrum shows that there are transitions readily accessible with the current setup in order to clearly identify acetylene which will be used to characterize the beam in dependence of parameters like discharge voltage, backing pressure and nozzle opening time. But before diving deeper into that the spectrum for diacetylene will be analyzed.

## 5.2 Diacetylene

Similarly to acetylene, a spectrum for mass 50 u can be extracted from the recorded data as explained earlier. As that mass is only visible in measurements with the discharge being turned on, the difference between discharge being turned on and off was computed for each wavelength, the area of the peak at 50 u was calculated and then plotted against the wavelength in order to generate a spectrum. This spectrum is shown in Figure 12. Here, three peaks are clearly visible at  $(41136 \pm 5.0) \text{ cm}^{-1}$ ,  $(43245 \pm 5.2) \text{ cm}^{-1}$  and  $(45343 \pm 5.4) \text{ cm}^{-1}$ , which are listed in Table 5. The given errors originate from the systematic error due to the wavelength uncertainty of the laser (assumed to be  $4.5 \pm \text{ cm}^{-1}$ ) and the statistical error from the fit. The error from the laser offset is not included. These three peaks have a distance of  $2109 \text{ cm}^{-1}$  and  $2098 \text{ cm}^{-1}$  in between, suggesting they might belong to the same vibrational progression. Indeed, references show that these transitions are from the ground state to the  $1^1\Delta_u$  state with the symmetric  $\text{C}\equiv\text{C-H}$  bending mode  $\nu_6$  being excited once [38]. The vibrational progression then comes from the symmetric  $\text{C}\equiv\text{C}$  stretching mode  $\nu_2$  which has  $2184 \text{ cm}^{-1}$  in the ground state. Aside from this progression, there are other peaks visible in the spectrum, though much weaker and almost hidden in the noise. Especially between  $41200$  and  $41600 \text{ cm}^{-1}$  some spectral structures can be suspected, which are not further analyzed.

The ionization threshold of diacetylene lies at  $(82064 \pm 30) \text{ cm}^{-1}$  [38]. This suggests that the electronic states are addressed via a 1+1-REMPI process. As the second peak is comparatively strong it allows diacetylene to be detected in the molecular beam.

Table 5: List of peaks shown in Figure 12 with their respective assignment.

Energy	Reference	Assignment
$(41136 \pm 5.0) \text{ cm}^{-1}$	$(41132 \pm 2.5) \text{ cm}^{-1}$ <sup>a</sup>	$1^1\Delta_u 6^1$
$(43245 \pm 5.2) \text{ cm}^{-1}$	$(43237 \pm 2.5) \text{ cm}^{-1}$ <sup>a</sup>	$1^1\Delta_u 2^1 6^1$
$(45343 \pm 5.4) \text{ cm}^{-1}$	$(45322 \pm 2.5) \text{ cm}^{-1}$ <sup>a</sup>	$1^1\Delta_u 2^2 6^1$

<sup>a</sup> 1+1-REMPI in a molecular beam [39]

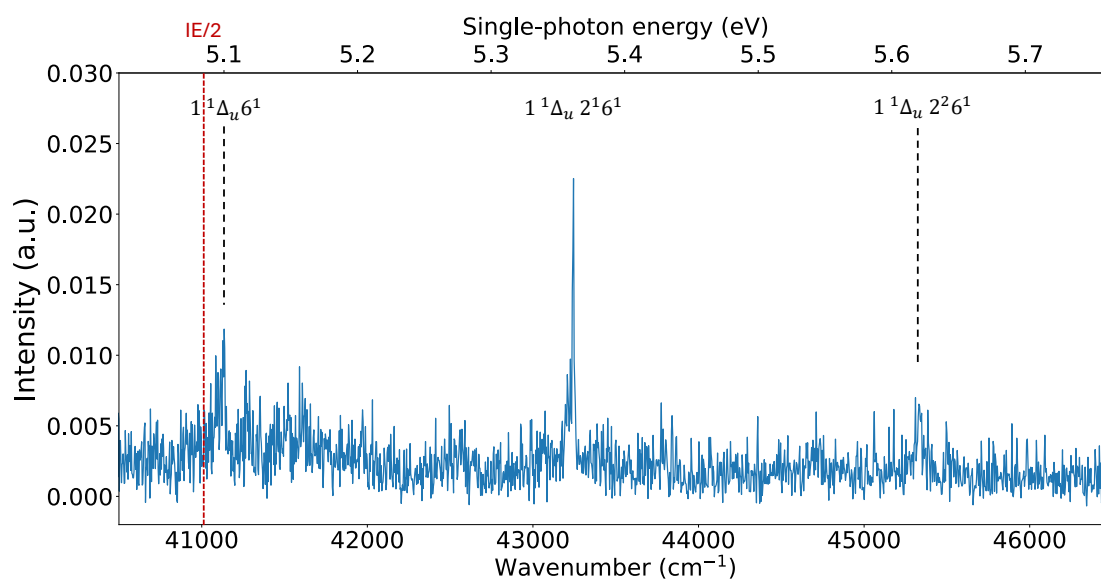


Figure 12: 1+1-REMPI spectrum of diacetylene in the range of 40500 cm<sup>-1</sup> to 46500 cm<sup>-1</sup>. Labeled peaks are transitions from the ground state  $\tilde{X}^1\Sigma_g^+$  to the respective state. As opposed to the acetylene spectrum, the electronic state is labeled as state 1, the lowest electronic state in diacetylene.

### 5.3 Density variations

Having accessible transitions to detect both acetylene and diacetylene allows the discharge and its yields to be characterized more thoroughly. In this experiment, the nozzle opening times were set between 25 to 36  $\mu\text{s}$  and the backing pressures were set to 1, 2, 5, and 10 bar, respectively. For each of these combinations the pulse ejected from the nozzle was probed by systematically varying the nozzle trigger in time in steps of 10  $\mu\text{s}$ , where 0  $\mu\text{s}$  denotes an arbitrary timestamp right before the pulse interacts with the laser beam with no signal being visible yet. This timestamp was kept constant for all measurements. A discharge voltage of 1100 V was applied for all measurements.

For each step, a narrow scan of 11 steps of 0.01 nm width over the respective peak was performed and a spectrum was generated from the data. For acetylene, the strongest peak, the  $3p\ ^1\Sigma_g^+$  state (269.15-269.25 nm) was used, and for diacetylene also the strongest peak, the  $1\ ^1\Delta_u2^16^1$  state (231.2-231.3 nm) was used. As excited helium was always present in the discharge for any wavelength, the helium yields were calculated from the acetylene range due to higher laser power in that range. To determine the yields from the spectra, the peak was fitted with a Voigt profile, from which the maximum could be computed. This was performed for acetylene and diacetylene individually. As the helium yield remained relatively constant within the measured range, the mean was taken instead. The results are plotted for each set of nozzle opening times and backing pressures as illustrated in Figure 13.

For a backing pressure of 1 bar it can be seen that for short opening times barely any diacetylene is formed. Only for an opening time of 30  $\mu\text{s}$  and longer a production of diacetylene can be seen which is the highest at 33  $\mu\text{s}$  and decreases again for 36  $\mu\text{s}$ . The maximum is shifted to higher times i.e. more to the back of the pulse, about 190  $\mu\text{s}$  for an opening time of 30  $\mu\text{s}$ , 170  $\mu\text{s}$  for an opening time of 33  $\mu\text{s}$  and 180  $\mu\text{s}$  for an opening time of 36  $\mu\text{s}$ . Meanwhile, the production of metastable helium also starts at 30  $\mu\text{s}$  and increases steadily until 36  $\mu\text{s}$ . The maximum is also shifted to the back of the pulse, about 150  $\mu\text{s}$  for all opening times. Acetylene can be seen in increasing amounts from 25  $\mu\text{s}$  to 36  $\mu\text{s}$  opening time with the exception of 28  $\mu\text{s}$  where a sudden decrease can be observed. The maximum is again shifted more to the back of the pulse, e.g. 230  $\mu\text{s}$  for an opening time of 27  $\mu\text{s}$ , but gradually shifts to 200  $\mu\text{s}$  for an opening time of 36  $\mu\text{s}$ , therefore being slightly behind the diacetylene maximum and notably behind the helium maximum.

For a backing pressure of 2 bar a similar behavior can be observed. Here, with opening times of 28  $\mu\text{s}$  diacetylene is slightly visible and increases until 33  $\mu\text{s}$ . However, with an

opening time of  $36\ \mu\text{s}$  three maxima can be seen. While the maximum lies around  $160\ \mu\text{s}$  for shorter opening times, here the maxima are shifted to  $130\ \mu\text{s}$ ,  $220\ \mu\text{s}$  and  $330\ \mu\text{s}$ . A small hint of this last maximum can already be seen with an opening time of  $33\ \mu\text{s}$ . Helium starts to be visible at  $28\ \mu\text{s}$  opening time and gradually increases until  $36\ \mu\text{s}$ . Its maximum gradually moves from  $170\ \mu\text{s}$  at  $28\ \mu\text{s}$  opening time towards  $140\ \mu\text{s}$  at  $33\ \mu\text{s}$  opening time and then suddenly jumps to  $190\ \mu\text{s}$  at  $36\ \mu\text{s}$  opening time also with a hint of a second maximum coming at  $340\ \mu\text{s}$ . Acetylene is already visible with short opening times like  $25\ \mu\text{s}$  and increases gradually until  $33\ \mu\text{s}$ . Starting at  $29\ \mu\text{s}$  opening time a second maximum at  $330\ \mu\text{s}$  emerges which gets more pronounced at  $33\ \mu\text{s}$  opening time. With an opening time of  $36\ \mu\text{s}$  the amount of acetylene detected drops to almost zero, just a small maximum at  $230\ \mu\text{s}$  can be observed.

For a backing pressure of 5 bar things change a little. Here, diacetylene can already be detected in small quantities with opening times of  $25\ \mu\text{s}$  and  $26\ \mu\text{s}$  which notably increases until  $29\ \mu\text{s}$ . At first, one maximum at  $170\ \mu\text{s}$  can be observed which abruptly moves to  $120\ \mu\text{s}$  at an opening time of  $27\ \mu\text{s}$ . Then, at  $29\ \mu\text{s}$  a second, smaller maximum at  $270\ \mu\text{s}$  appears. These two maxima remain for longer opening times, but the overall amount of diacetylene decreases. While those two maxima have roughly the same intensity at an opening time of  $30\ \mu\text{s}$ , the first maximum decreases a little more than the second for opening times of  $33\ \mu\text{s}$  and  $36\ \mu\text{s}$ . Helium can also be observed for short opening times like  $25\ \mu\text{s}$  and  $26\ \mu\text{s}$  whose amounts increase until  $33\ \mu\text{s}$  and decrease again at  $36\ \mu\text{s}$ . At  $33\ \mu\text{s}$  it exhibits a second maximum towards the back of the pulse which is retained for  $36\ \mu\text{s}$ . Acetylene can also be observed for short opening times. The amounts increase gradually until  $30\ \mu\text{s}$  and then suddenly drop to almost zero for  $33\ \mu\text{s}$  and  $36\ \mu\text{s}$ . Starting from  $28\ \mu\text{s}$  it gains a second maximum at the back of the pulse.

For a backing pressure of 10 bar, diacetylene, helium and acetylene can all be observed for the shortest opening time of  $25\ \mu\text{s}$  where diacetylene has its maximum at around  $120\ \mu\text{s}$ . At an opening time of  $26\ \mu\text{s}$  it gains a second maximum at  $240\ \mu\text{s}$  which gets more pronounced for longer opening times. At  $28\ \mu\text{s}$  it seems to split up into two maxima at  $200\ \mu\text{s}$  and  $280\ \mu\text{s}$ . At  $29\ \mu\text{s}$  almost nothing can be observed, which stands out from the other measurements and will be discussed in a later section. At  $30\ \mu\text{s}$  the three maxima remain, though the yield is diminished, and a fourth maximum can be seen at the very end of the measured range. For longer opening times the yield decreases significantly. The helium yield also increases from  $25\ \mu\text{s}$  until  $28\ \mu\text{s}$  and then decreases from  $30\ \mu\text{s}$  to  $36\ \mu\text{s}$  opening time while the maximum does not seem to shift much. At  $30\ \mu\text{s}$  a second maximum emerges which is not seen for any other opening time. Acetylene is only visible with

increasing amounts until  $27 \mu\text{s}$  after which it disappears completely. Until then it exhibits two maxima at  $140 \mu\text{s}$  and  $250 \mu\text{s}$ .

As particle density and voltage play an important role in electrical discharges these parameters have to be discussed. While the voltage was kept constant at 1100 V only the particle density was varied during these measurements. Shorter opening times and lower backing pressures both decrease the particle density during expansion while longer opening times and higher backing pressures increase it. Low particle densities, such as for  $25\text{-}29 \mu\text{s}$  and 1 bar show almost no diacetylene yield and also no helium yield indicating insufficient particle amounts for a sufficient discharge to be formed. This changes for an opening time of  $30 \mu\text{s}$  and more, where the particle density seems high enough to form a discharge. Especially the opening time of  $33 \mu\text{s}$  shows a good amount of diacetylene being produced while almost no metastable helium is visible. Its maximum is slightly shifted to the front of the pulse compared to acetylene suggesting that the density of acetylene is sufficient there. When the acetylene maximum is reached, the diacetylene production already starts to decrease. This becomes even more obvious for an opening time of  $36 \mu\text{s}$ , where a high amount of acetylene is visible but comparably low amounts of diacetylene can be observed. Here, a suitable density of acetylene seems to be reached only very briefly leading to a diminished production of diacetylene in the discharge. When comparing the maxima of helium, acetylene and diacetylene, it should be noted, that even though it can safely be assumed that acetylene is evenly distributed in the carrier gas, the pulse has to travel roughly one meter after leaving the nozzle. During that distance, it is possible that the molecular beam separates itself so that lighter masses reach the interaction chamber slightly earlier than heavier masses. This would result in helium coming earlier in the pulse than acetylene and diacetylene. For 1 bar backing pressure this can be observed for helium at  $33 \mu\text{s}$  and  $36 \mu\text{s}$  opening time. However, as already mentioned, the diacetylene peak comes earlier than the acetylene peak, possibly due to the density being optimal at the rising flank of acetylene. A backing pressure of 2 bar draws a similar picture with no amount of diacetylene being visible until  $28 \mu\text{s}$ . Helium only starts being visible at  $29 \mu\text{s}$  and also similar to a backing pressure of 1 bar, it comes earlier within the pulse than acetylene with a time difference of roughly  $40\text{-}60 \mu\text{s}$ . The amount of helium becomes comparably strong for an opening time of  $33 \mu\text{s}$  and much stronger for  $36 \mu\text{s}$ . At least for helium, it seems like the production conditions for metastable helium are optimal here. However, the production conditions for diacetylene are not as good which can be observed as the amount of diacetylene decreases from  $33 \mu\text{s}$  to  $36 \mu\text{s}$ . Three maxima are visible suggesting that a suitable density is reached more than just once throughout the

gas expansion. As the density during the expansion increases and decreases again and the discharge voltage recovers quickly enough an optimal density to allow a discharge can occur twice at maximum. Now that there are three maxima visible it can be assumed that the nozzle does not shut completely after its initial opening but instead releases secondary pulses. The most striking fact is that for long opening times, no acetylene is visible anymore. One possible reason is that, in conjunction with a lot of metastable helium being formed in the discharge, most of the acetylene is being destroyed there and other species are formed. The three diacetylene maxima indicate that there had to be acetylene present in the discharge and reactions must have happened even though it could not be detected via the REMPI process.

The measurements with a backing pressure of 5 bar again start with low amounts of helium and acetylene being visible. Starting at an opening time of  $27 \mu\text{s}$  a diacetylene peak emerges which again has its maximum earlier in the pulse than the acetylene maximum. The helium maximum even comes a little earlier within the pulse which supports the hypothesis of the masses slightly separating over time. Again, the diacetylene peak sits at the rising flank of the acetylene peak. This continues until the density becomes less optimal for diacetylene being formed, here at  $30 \mu\text{s}$  and above. As with 2 bar backing pressure, the acetylene is no longer visible for  $33 \mu\text{s}$  and above while the diacetylene exhibits two peaks which loosely match with the helium peaks indicating that again enough acetylene was broken down to form new species in the discharge. For most of the opening times and a backing pressure of 10 bar the same behavior can be observed. Acetylene forms two maxima quite early which is loosely matched by diacetylene although again some microseconds earlier in the pulse. Acetylene vanishes at an opening time of  $28 \mu\text{s}$  and above likely due to the same reasons like already mentioned. This is backed by the observation that there is still diacetylene being formed at opening times of  $30 \mu\text{s}$  and  $33 \mu\text{s}$ . After that, only helium is visible.

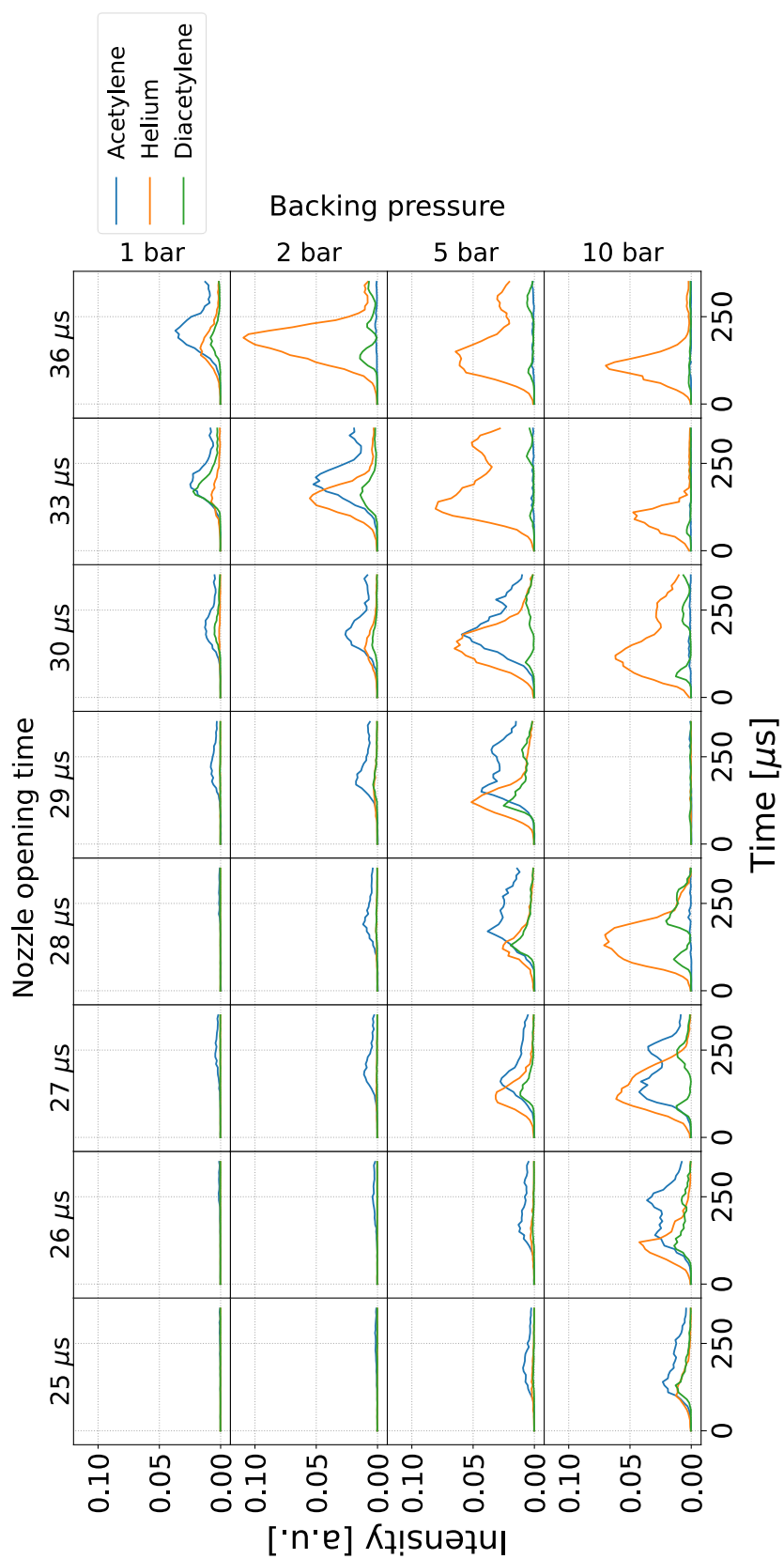


Figure 13: Amounts of acetylene, diacetylene and helium within the gas pulse for varying nozzle opening times and backing pressures of 0.5% acetylene in helium. A voltage of 1100 V was used together with a discharge delay of  $-150 \mu\text{s}$  and a discharge pulse length of  $700 \mu\text{s}$ . Due to changes to the experiment the measurement with 10 bar and  $29 \mu\text{s}$  did not show any signal.

In Figure 14 the diacetylene yields for different pressures and opening times are shown. The yields were acquired by calculating the area under the respective diacetylene graphs in Figure 13 using Python. It shows that for each backing pressure, an optimal opening time can be found which lies around  $33 \mu\text{s}$  for 1 bar of backing pressure, around  $36 \mu\text{s}$  for 2 bar of backing pressure, around  $29 \mu\text{s}$  for 5 bar of backing pressure and around  $28 \mu\text{s}$  for 10 bar of backing pressure. While the optimal opening time seems to increase at first for increasing backing pressures, it drops to shorter times for higher pressures. There, the yields are also notably higher, although that might be a consequence of several diacetylene maxima being formed in the pulse. Another parameter playing a critical role in discharge processes is obviously the applied voltage to the electrodes, which will be demonstrated in the next chapter.

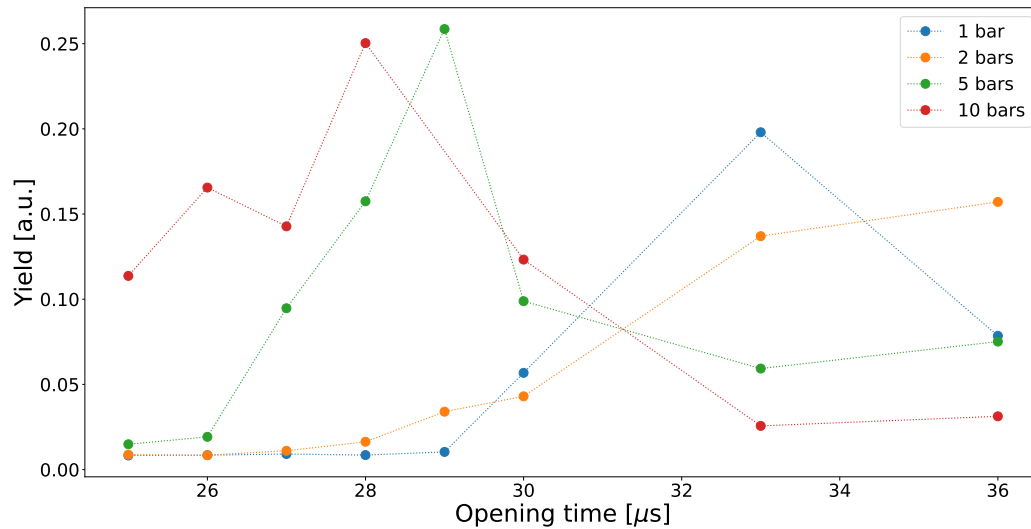


Figure 14: Total diacetylene yields with different nozzle opening times at varying backing pressures. The lines between the measured data have no physical meaning and are only shown for clarity.

## 5.4 Voltage variations

The previous experiments have been performed with a voltage fixed at 1100 V due to good results in other experiments. Depending on the daily conditions, the discharge was visibly working at voltages above 750 V. A hysteresis behaviour could be observed when a higher voltage was applied and gradually decreased, then voltages around 650 V could be achieved on good days. In order to determine the yield of diacetylene, a similar procedure as in the previous experiment was performed. Again, a narrow scan of 11 steps from 231.2 nm to 231.3 nm was done, the difference between discharge turned on and off was calculated, and the maximum of the peak was taken by fitting a Voigt profile. As the acetylene "yield" was not considered relevant for the voltage dependence, no scan over the respective peak was done. Metastable helium again is present at all wavelengths via non-resonant ionization whenever the discharge is turned on and can therefore be measured simultaneously. Within the measured range, the helium yield can be assumed constant and a linear fit was used to determine it. For this experiment, the voltage was set to 700 V when no discharge was visible and increased in steps of 20 V until a voltage of 1440 V was reached. The voltage was measured with an oscilloscope attached to the voltage supply. For each of the measurements, a backing pressure of 5 bar and an opening time of 29  $\mu\text{s}$  was used.

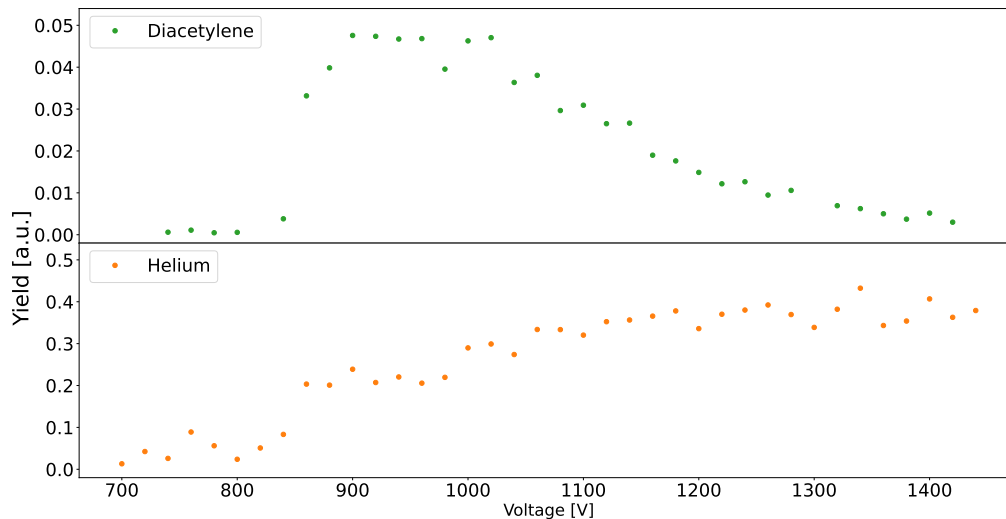


Figure 15: Yields of helium and diacetylene in dependence of the voltage. A backing pressure of 5 bar and an opening time of 29  $\mu\text{s}$  was used and the measured position inside the pulse was set at 140  $\mu\text{s}$ .

Figure 15 shows the yields of both helium and diacetylene in dependence of the applied voltage. It can be observed that the discharge starts running consistently above a voltage of 840 V where the yields of helium and diacetylene both start rising. The helium yield then consistently increases with increasing voltage though the curve flattens towards higher voltages. In contrast, the diacetylene yield reaches a plateau at a voltage of 900 V which is sustained until 1000 V and then gradually decreases. At a voltage of 1300 V barely any diacetylene can be observed anymore. A possible reason for this, is that a higher voltage leads to a higher energy of particles involved in the discharge process. Greater amounts of electrons and ionized helium may negatively impact the formation of bigger molecules. During the supersonic expansion, these charged particles interact with each other and with the neutral acetylene, which can lead to bond breaking. These resulting fragments can react with other and form new molecules, which not necessarily have to be stable. A higher amount of ionized helium or helium with more energy may cause more transient species to be destroyed again before they even reach the zone of silence where no interaction occurs anymore.

## 6 Discussion

The main focus of this work was to employ the Even-Lavie valve with the mountable discharge nozzle and to gain insight on the production of hydrocarbon species from discharged acetylene. As shown before, the production of diacetylene was sufficient to gain a spectrum with electronic transitions from which a more thorough investigation on the yields was possible. Other comparably strong masses like 36 u, 37 u or 49 u did not show any spectral signature within the measured range, further complicating a viable detection via REMPI, which demands an electronic transition to detect the molecule. Other, even weaker masses also did not show any transitions in the spectrum. They can still be observed due to MPI, where no transition is needed for detection.

### Mass spectra

The mass spectrum is generated from the MCP with a voltage of 2000 V applied. Strong signals can therefore show an electronic ringing which causes the signal to drop below zero after the actual mass signal. This happens due to an electronic oscillation on the MCP whenever a signal is detected and scales with signal strength. Therefore it does not play a role for most signals in the mass spectrum, except for stronger ones like helium, acetylene and diacetylene. Depending on how long the oscillation is, it may interfere with a possible signal on a subsequent mass channel. While the helium signal shows a strong electronic ringing in Figures 9 and 10, the mass channel of 5 u is still distant enough and would most likely not have any relevance for the experiment due to only carbon and hydrogen being used as precursor elements. The acetylene signal also shows some electronic ringing, though the oscillation is not sustained long enough to interfere with the 27 u mass channel. However, the diacetylene signal shows a strong ringing, especially in Figure 10, which is strong enough to mask a potential 51 u mass channel. Another factor that can have an influence on the mass spectrum is a timing jitter. As the laser emission does not happen exactly at the same time after the laser received its trigger signal, but varies by several nanoseconds, the same mass channel is shifted back and forth by a few nanoseconds with each measurement step if the digitizer is triggered consistently at the same time. This leads to a broadening and flattening of the averaged signal. Employing an external photodiode which captures scattered light from the laser beam allows to trigger the digitizer only when light is emitted, therefore eliminating the laser-induced jitter. Other effects potentially impairing the mass spectrum were not observed.

It should be noted that the two mass spectra were recorded under different conditions including backing pressure, nozzle opening time, voltage, and acetylene concentration. The first measurement with 5 bar of 2 % acetylene in helium and an opening time of 40  $\mu$ s was conducted to have high amounts of acetylene available for reaction. Based on results from previous experiments a voltage of 900 V was chosen. The more diluted mixture with 0.5 % acetylene in helium in conjunction with a higher voltage of 1100 V seems to yield more diacetylene which has also been used by Zhao et al. though with a general valve instead [40]. As already explained in chapter 5.1 the scanning ranges between these two experiments varied greatly, leading to the introduction of the correction factor of  $\sqrt{\frac{3501}{2701}} \approx 1.14$ . However, the laser power, which varies with its wavelength, is lower at shorter wavelengths and higher at longer wavelengths. Therefore, the second spectrum shown in Figure 10 and recorded at 210-280 nm benefits from the higher laser power in the range of 237-280 nm increasing the overall signal. To improve comparability between these two experiments, a laser power curve can help calibrating the spectra assuming a linear scaling of signal strength with laser power.

As shown in the mass spectra, the discharge produces not only hydrocarbons but also soot which consists mostly of amorphous carbon and can have an influence on the experiment. Soot can increase the voltage needed to initiate the discharge by clogging the valve up to a point when no discharge can be done anymore. Gentle cleaning of the valve allows the experiment to be run again. The whole measurement campaign presented in chapter 5.3 was performed without cleaning the nozzle once in between except for the measurement with 10 bar of backing pressure and 29  $\mu$ s opening time, which was done after a cleaning procedure. As there was almost no signal to be seen, there are some reasons for that. One reason could be, that the presence of soot enhances the formation of diacetylene or even other hydrocarbon species as the other measurements were conducted with soot present in the valve. All in all, repeating this measurement would help, best after some soot has built up in the valve to get comparable results.

In the background subtracted mass spectra not only new species can be observed but also the precursor molecule acetylene. This is particularly surprising as the biggest amount of acetylene should be present when the discharge is turned off. Yet a fairly strong signal is visible suggesting that there is more acetylene present when the discharge is turned on. One possible reason could be that the discharge affects the acetylene so that enough molecules remain in an excited state which is already being observed with helium. That makes an ionization via MPI more likely as fewer photons are needed to reach the ionization energy. This effect can also add up over the broad scanning range and, similarly

to helium, should scale with voltage as shown in Figure 15. However, an increased voltage involves different production conditions and therefore may influence the amount of acetylene produced via fragmentation.

## Acetylene spectrum

In the acetylene spectrum shown in Figure 11, nine peaks have been assigned. For most of them, there was a clear and relatively consistent offset visible compared to their reference ranging between  $13$  and  $24\text{ cm}^{-1}$ , which may originate from the internal wavelength offset of the laser source. This can be confirmed even for the already existing data by using a spectrum analyzer to create a reference for any given wavelength within the measured range and then recompute the spectrum with the updated wavelengths. A two-photon process at  $(74000 \pm 13 - 24)\text{ cm}^{-1}$  translates to a single-photon wavelength of  $(270.27 \pm 0.05 - 0.09)\text{ nm}$ , which is a reasonable offset in that wavelength range.

The varying power of the laser within the measured range also has an influence on the spectrum. At  $84200\text{ cm}^{-1}$ , the laser pulse energy usually lies around  $10\text{ }\mu\text{J}$  while it ranges at roughly  $15\text{ }\mu\text{J}$  at  $71700\text{ cm}^{-1}$ . This leads to peaks at a lower wavenumber appearing stronger than peaks at a higher wavenumber. In the spectrum, none of the peaks are rotationally resolved. This was to be expected as the spectral width of the laser is around  $5 - 9\text{ cm}^{-1}$  within the measured range while the  $2B$  distance for acetylene is around  $2.3\text{ cm}^{-1}$ . Therefore, no rotational resolution can be seen. Nonetheless, the shapes of most peaks are quite narrow and do not show any signs of additional Doppler or power broadening. The  $3p\text{ }^1\Sigma_g^+$  progression is limited only to the vibrational ground state and the  $\nu_2$  being excited once with no other vibrational modes coupling. This matches with the observations of Tsuji et al. [36] who measured jet-cooled acetylene via a two-photon fluorescence excitation scheme in that range by monitoring the corresponding Swan system. Other vibronically excited states may not be visible due to small Franck-Condon factors. The  $3p\text{ }^1\Delta_g$  progression shows more vibrationally excited states, which involve the  $\nu_2$  and  $\nu_4$  modes.

## Diacetylene spectrum

The spectrum of diacetylene shown in Figure 12 has three stronger peaks which have been assigned according to [39]. The peaks all belong to the  $1^1\Delta_u$  state with its vibrational progression in the  $\nu_2$  and  $\nu_6$  modes which lie just above half of the ionization energy. Other peaks in that region have not been assigned but were identified as transitions into other vibrationally excited states of the same electronic state [39] including the C-C symmetric stretching mode  $\nu_3$  and the C $\equiv$ C-C symmetric bending mode  $\nu_7$ . The band origin is estimated to be at  $40845\text{ cm}^{-1}$ . Bandy et al. state that higher states of  $^1\Sigma_u^+$  or  $^1\Pi_u$  symmetry carry oscillator strength from the ground state which can induce intensity into the  $^1\Delta_u$  state through vibronic coupling.

The error range of the reference originates from a graphical analysis of their spectrum [39]. Comparing this to the measured peaks in this work shows, that the data here matches the reference quite well for the first two peaks but not for the third. One reason could be that the peaks in the reference are becoming increasingly broad, complicating to find the exact center of the peak. Another reason could be the offset of the laser as mentioned earlier.

## Density variations

When varying the backing pressure and the nozzle opening time, several maxima of acetylene, diacetylene and helium could be observed as shown in Figure 13. They tend to emerge for longer opening times and higher backing pressure and have been studied by Steven Ingunza more thoroughly in his thesis [41]. He showed that the valve opens at least two times after a trigger pulse is received, with full-width half-maximum (FWHM) values depending on both pressure and opening time. The amount of secondary openings also depend on both pressure and opening time, with three openings being visible for opening times of  $24\ \mu\text{s}$  and longer at a backing pressure of 15 bar. A backing pressure of 25 bar even showed four openings in total. Therefore, these secondary openings are to be expected in this work and can be observed for various measurements in Figure 13. It should be noted, that the gas pulse in the reference was measured within a distance of 3 cm from the nozzle while the distance between the nozzle and the laser interaction point amounts to roughly 1 m. Thus, the gas pulse can smear out over the travel distance so the single openings may blend into each other, which is indeed observed. For 15 bar and  $27\ \mu\text{s}$  the first opening showed a FWHM of around  $100\ \mu\text{s}$  in the reference which roughly matches the current observations at 10 bar.

The long distance between nozzle and interaction chamber also leads to a slight mass separation within the gas pulse. This has been investigated by Kato et al. [42] with argon-helium mixtures of different molar fractions, where heavier argon atoms are accelerated due to the seeding effect induced by lighter helium atoms. Still, after a distance of 60 cm, a slight mass separation of the argon-helium mixture could be observed in the range of several  $\mu\text{s}$ . Therefore, the reason why helium always arrives earlier at the interaction chamber than acetylene and diacetylene probably arises from that phenomenon.

### **Voltage variations**

Varying the voltage clearly shows different results for helium and diacetylene as presented in Figure 15. While diacetylene is produced the most at comparably low voltages between 860 V and 1100 V, indicating that the chemistry happening during the supersonic expansion indeed is strongly affected by the voltage. However, the effect on other masses being produced at higher or lower voltages in the experiment remains unknown and is subject to further investigations.

A parameter which has not been taken into account systematically for these measurements is the discharge pulse length. Usually it was set to durations which are significantly longer than the nozzle opening time, allowing the voltage to recover quickly and to be provided almost constantly during the gas pulse ejection. This can lead to multiple discharges shortly after another which can have an influence on the production of diacetylene and other species. Shortening this duration in conjunction with voltage adjustments may alter the yields of various hydrocarbons in a yet unknown way.

## 7 Conclusion and Outlook

In this work, the mountable pulsed discharge nozzle in conjunction with the Even-Lavie valve paired with a REMPI-ToF mass spectrometer was employed to investigate the yields of hydrocarbon species from an acetylene discharge. The focus of this work laid on diacetylene due to its accessibility via the REMPI scheme. First, two mass spectra of discharged acetylene in helium were recorded, one with high particle density and a higher fraction of acetylene, and one with lower particle density and a lower fraction of acetylene. The measurement with higher amounts of acetylene favored the formation of bigger hydrocarbons more, while the other measurement with lower amounts of acetylene favors the formation of smaller hydrocarbons, diacetylene in particular, more. Hydrocarbon species up to  $C_8H_n$  have been observed in the spectrum, while species with even amounts of carbon atoms tend to occur more often. Only diacetylene and acetylene showed wavelength-dependent spectral signatures, which were analyzed. Diacetylene only showed transitions into some of the vibrationally excited  $1^1\Delta_u$  state. Here, only the  $\nu_2$  progression coupled with one quantum in the  $\nu_6$  was assigned, other signals in the spectrum, probably belonging to the same electronic state, were too weak to analyze. Acetylene showed a richer spectrum with various transitions into electronic states of the 3p orbital. Some low vibrationally excited states could be observed as well with coupling of the  $\nu_2$  and the  $\nu_4$  modes. The strongest peaks of the spectra were used to determine the yields and they were compared for different production conditions. They were varied by setting the backing pressure of the 0.5% acetylene in helium mixture to 1, 2, 5, and 10 bar respectively, each with nozzle opening times of 25-30, 33, and 36  $\mu s$  at a constant voltage of 1100 V. The ejected pulse was scanned step-wise by changing the time delay between the pulse ejection and laser interaction. These measurements have shown that the biggest total yield of diacetylene was achieved for higher pressures with opening times of 28-29  $\mu s$  though with the drawback of the diacetylene being distributed within the pulse over two maxima. For lower pressures, an opening time of 33  $\mu s$  brought slightly lower yields. More insight on both the yield and the nozzle behavior can be gained by scanning the opening times above 30  $\mu s$  in smaller steps.

The ability of the REMPI-ToF mass spectrometer to give spectral information on specific mass channels allows the determination of the temperature of the species formed in the discharge. By employing a laser with a more narrow linewidth, the rotational structure of the transitions could be resolved and, given a suitable simulation, the temperature can be estimated, which most likely differs significantly from the 1 K observed with the basic

Even-Lavie valve.

To conclude, the method successfully determined the yields of diacetylene in a discharge via REMPI and can be extended to other species, provided a suitable electronic transition is identified. This procedure is not limited to hydrocarbons produced from acetylene but can be employed for basically any precursor molecule in gas phase. Introducing other elements like nitrogen, oxygen or sulfur expands the range of possible transient molecules. However, this quickly complicates spectral analysis as multiple species may have overlapping masses. Nevertheless, this procedure has shown that once a suitable electronic transition is found, it is possible to pinpoint the molecule and optimize the production conditions around it. These findings enable further experiments under optimized production conditions, e.g. to work towards the identification of new DIB carriers by providing controlled environments for their spectral analysis. Within this work, a systematic way of production and identification of hydrocarbons in a discharge has been shown, followed by a systematic optimization scheme of the production conditions that further experiments can make use of, if more complex molecules are aimed to be analyzed.

## References

- [1] T. R. Geballe, “The diffuse interstellar bands - a brief review”, *Journal of Physics: Conference Series* **728**, 062005 (2016).
- [2] M. C. McCarthy, K. L. K. Lee, P. B. Carroll, J. P. Porterfield, P. B. Changala, J. H. Thorpe, and J. F. Stanton, “Exhaustive Product Analysis of Three Benzene Discharges by Microwave Spectroscopy”, *The journal of physical chemistry. A* **124**, 5170–5181 (2020).
- [3] C. Feng, L. Wang, Y. Wang, L. Gao, and H. Ding, “Diagnosis of Active Species in Reactive Acetylene Plasma by Laser-Ionization Molecular-Beam Time-of-Flight Mass Spectrometry”, *Plasma Chemistry and Plasma Processing* **31**, 405–415 (2011).
- [4] A. H. Laufer and A. Fahr, “Reactions and kinetics of unsaturated C<sub>2</sub> hydrocarbon radicals”, *Chemical reviews* **104**, 2813–2832 (2004).
- [5] H. Fan, L. M. Hobbs, J. A. Dahlstrom, D. E. Welty, D. G. York, B. Rachford, T. P. Snow, P. Sonnentrucker, N. Baskes, and G. Zhao, “The Apache Point Observatory Catalog of Optical Diffuse Interstellar Bands”, *The Astrophysical Journal* **878**, 151 (2019).
- [6] L. Schlarman, B. Foing, J. Cami, and H. Fan, “C<sub>60</sub>+ diffuse interstellar band correlations and environmental variations”, *Astronomy & Astrophysics* **656**, L17 (2021).
- [7] N. L. Cox, “The PAH-DIB Hypothesis”, *EAS Publications Series* **46**, 349–354 (2011).
- [8] W. Gerlach and O. Stern, “Der experimentelle Nachweis der Richtungsquantelung im Magnetfeld”, *Zeitschrift für Physik* **9**, 349–352 (1922).
- [9] John R. Arthur, “Molecular beam epitaxy”, *Surface Science* **500**, 189–217 (2002).
- [10] R. Campargue, *Atomic and Molecular Beams: The State of the Art 2000* (Springer Berlin Heidelberg, 2012).
- [11] M. Barr, K. M. O’Donnell, A. Fahy, W. Allison, and P. C. Dastoor, “A desktop supersonic free-jet beam source for a scanning helium microscope (SHeM)”, *Measurement Science and Technology* **23**, 105901 (2012).
- [12] A. G. Atkins and M. P. Escudier, *A dictionary of mechanical engineering: Over 8,500 definitions for students and professionals*, Oxford paperback reference (Oxford University Press, Oxford, 2013).

- [13] D. M. Lubman, C. T. Rettner, and R. N. Zare, “How Isolated Are Molecules In a Molecular Beam?”, *The Journal of Physical Chemistry* **1982**, 1129–1135 (1982).
- [14] P. A. Tipler and G. Mosca, *Physik für Wissenschaftler und Ingenieure*, 6., dt. Aufl. (Spektrum Akad. Verl., Heidelberg, 2009).
- [15] P. A. Thompson, *Compressible-fluid dynamics*, Advanced engineering series (McGraw-Hill, New York, 1972).
- [16] G. K. Batchelor, *An Introduction to fluid dynamics*, 14. print, Cambridge mathematical library (Cambridge Univ. Press, Cambridge, 2010).
- [17] P. Straňák, L. Ploenes, S. Hofsäss, K. Dulitz, F. Stienkemeier, and S. Willitsch, “Development and characterization of high-repetition-rate sources for supersonic beams of fluorine radicals”, *The Review of scientific instruments* **92**, 103203 (2021).
- [18] A. Fridman, *Plasma Chemistry* (Cambridge University Press, 2009).
- [19] J. T. Gudmundsson and A. Hecimovic, “Foundations of DC plasma sources”, *Plasma Sources Science and Technology* **26**, 123001 (2017).
- [20] A. Piel, *Plasma Physics* (Springer International Publishing, Cham, 2017).
- [21] P. F. Bernath, *Spectra of atoms and molecules*, 2. ed. (Oxford University Press, New York, 2005).
- [22] G. Herzberg, *Electronic spectra and electronic structure of polyatomic molecules*, Vol. 3, *Molecular spectra and molecular structure / by Gerhard Herzberg* (van Nostrand, New York, NY, 1966).
- [23] K. L. Chubb, J. Tennyson, and S. N. Yurchenko, “ExoMol molecular line lists – XXXVII. Spectra of acetylene”, *Monthly Notices of the Royal Astronomical Society* **493**, 1531–1545 (2020).
- [24] H. Haken and H. C. Wolf, *Atom- und Quantenphysik: Einführung in die experimentellen und theoretischen Grundlagen*, Achte, aktualisierte und erweiterte Auflage, Springer-Lehrbuch (Springer, Berlin and Heidelberg, 2004).
- [25] “Bakerian Lecture: -Rays of positive electricity”, *Proceedings of the Royal Society of London. Series A, Containing Papers of a Mathematical and Physical Character* **89**, 1–20 (1913).
- [26] “Sitzungsberichte der königlichen Akademie der Wissenschaften zu Berlin, Juli 1886”, *Annalen der Physik und Chemie* **64**, 691–699 (1898).

- [27] W. Wien, “Untersuchungen über die electriche Entladung in verdünnten Gasen”, *Annalen der Physik* **301**, 440–452 (1898).
- [28] A. J. Dempster, “A new Method of Positive Ray Analysis”, *Physical Review* **11**, 316–325 (1918).
- [29] F. Aston, “LXXIV. A positive ray spectrograph”, *The London, Edinburgh, and Dublin Philosophical Magazine and Journal of Science* **38**, 707–714 (1919).
- [30] A. E. Cameron and J. Eggers D. F., “An Ion “Velocitron””, *Review of Scientific Instruments* **19**, 605–607 (1948).
- [31] W. C. Wiley and I. H. McLaren, “Time-of-Flight Mass Spectrometer with Improved Resolution”, *Review of Scientific Instruments* **26**, 1150–1157 (1955).
- [32] B. A. Mamyurin, V. I. Karataev, D. V. Shmikk, and V. A. Zagulin, “The mass-reflectron, a new nonmagnetic time-of-flight mass spectrometer with high resolution”, *Zh. Eksp. Teor. Fiz* **64**, 82–89 (1973).
- [33] A. Makarov, *Electrostatic Axially Harmonic Orbital Trapping: A High-Performance Technique of Mass Analysis*, Feb. 2000.
- [34] U. Even, ““the even-lavie valve as a source for high intensity supersonic beam””, *EPJ Techniques and Instrumentation* **2** (2015).
- [35] R. Dressler and M. Allan, “A dissociative electron attachment, electron transmission, and electron energy-loss study of the temporary negative ion of acetylene”, *The Journal of Chemical Physics* **87**, 4510–4518 (1987).
- [36] K. Tsuji, N. Arakawa, A. Kawai, and K. Shibuya, “Spectroscopy and Predissociation of Acetylene in the  $np$  Gerade Rydberg States”, *The Journal of Physical Chemistry A* **106**, 747–753 (2002).
- [37] M. Takahashi, M. Fujii, and M. Ito, “Two-color double resonance spectroscopy via  $\tilde{A}^1A_u$  state of acetylene:  $3p$  Rydberg state and its Renner–Teller effect”, *The Journal of Chemical Physics* **96**, 6486–6494 (1992).
- [38] C. Ramos, P. R. Winter, T. S. Zwier, and S. T. Pratt, “Photoelectron spectroscopy via the  $1^1\Delta_u$  state of diacetylene”, *The Journal of Chemical Physics* **116**, 4011–4022 (2002).
- [39] R. E. Bandy, C. Lakshminarayan, and T. S. Zwier, “Spectroscopy and photophysics of the  $1.DELTA.u$  .rarw.  $1.SIGMA.g+$  transition of jet-cooled diacetylenes ( $C_4H_2$ ,  $C_4HD$ , and  $C_4D_2$ )”, *The Journal of Physical Chemistry* **96**, 5337–5343 (1992).

- 
- [40] D. Zhao, K. D. Doney, and H. Linnartz, “High-resolution infrared spectra of vibrationally excited HC<sub>4</sub>H in a supersonic hydrocarbon plasma jet”, *Journal of Molecular Spectroscopy* **296**, 1–8 (2014).
- [41] S. Ingunza, “Charakterisierung einer Even-Lavie-Düse”, unpublished thesis (2018).
- [42] S. KATO, N. TSUJINO, M. KATAGIRI, and T. FUJIMOTO, “The Effects of Seeding and Mass Separation in Molecular Beams of a He-Ar Mixture”, *JSME international journal. Ser. 2, Fluids engineering, heat transfer, power, combustion, thermo-physical properties* **32**, 25–31 (1989).

## **Declaration of own work**

I hereby confirm that I have written this master's thesis independently and have used only the tools explicitly stated. All passages taken from other works, whether in wording or meaning, have been clearly identified and properly acknowledged.

---

Sebastian Schwetje